

LLE Review

Quarterly Report



About the Cover:

Based on NIF technology and developed with the assistance of LLNL scientists, a new plasma-electrode Pockels cell (PEPC) was developed at LLE for the OMEGA EP system. The need for target retro isolation, arising from OMEGA EP's short-pulse mission, imposes a very high-contrast requirement that necessitates the high-contrast PEPC development effort, results of which are reported in this issue. The cover photo shows the OMEGA EP production PEPC with Project Coordinator Zachary Hoyt in the foreground and Principal Investigator Brian Kruschwitz in the background. The inside photo shows key members of the PEPC development team (left to right: Zachary Hoyt, Troy Walker, Steve Reber, and Emil Cost) preparing the PEPC test stand—a full-aperture, time-resolved polarimeter—for an experiment.



This report was prepared as an account of work conducted by the Laboratory for Laser Energetics and sponsored by New York State Energy Research and Development Authority, the University of Rochester, the U.S. Department of Energy, and other agencies. Neither the above named sponsors, nor any of their employees, makes any warranty, expressed or implied, or assumes any legal liability or responsibility for the accuracy, completeness, or usefulness of any information, apparatus, product, or process disclosed, or represents that its use would not infringe privately owned rights. Reference herein to any specific commercial product, process, or service by trade name, mark, manufacturer, or otherwise, does not necessarily constitute or imply its endorsement, recommendation, or favoring

by the United States Government or any agency thereof or any other sponsor. Results reported in the LLE Review should not be taken as necessarily final results as they represent active research. The views and opinions of authors expressed herein do not necessarily state or reflect those of any of the above sponsoring entities.

The work described in this volume includes current research at the Laboratory for Laser Energetics, which is supported by New York State Energy Research and Development Authority, the University of Rochester, the U.S. Department of Energy Office of Inertial Confinement Fusion under Cooperative Agreement No. DE-FC03-92SF19460, and other agencies.

Printed in the United States of America
Available from
National Technical Information Services
U.S. Department of Commerce
5285 Port Royal Road
Springfield, VA 22161
Price codes: Printed Copy A03
Microfiche A01

For questions or comments, contact Jake Bromage, Editor, Laboratory for Laser Energetics, 250 East River Road, Rochester, NY 14623-1299, (585) 273-5105.

Worldwide-Web Home Page: <http://www.lle.rochester.edu/>

LLE Review

Quarterly Report



Contents

In Brief	iii
High-Contrast Plasma-Electrode Pockels Cell (PEPC)	129
Absolute Calibration of Kodak Biomax-MS Film Response to X Rays in the 1.5- to 8-keV Energy Range	138
Response Model for Kodak Biomax-MS Film to X Rays	142
High-Yield Bang Time Detector for the OMEGA Laser	147
Operation of Target Diagnostics in a Petawatt Environment	153
Gain Apodization in Highly Doped, Distributed-Feedback (DFB) Fiber Lasers	160
Publications and Conference Presentations	

In Brief

This volume of the LLE Review, covering April–June 2006, features “High-Contrast Plasma-Electrode Pockels Cell (PEPC)” by B. E. Kruschwitz, J. H. Kelly, M. J. Shoup III, L. J. Waxer, E. C. Cost, E. T. Green, Z. M. Hoyt, J. Taniguchi, and T. W. Walker. In this article (p. 129), the authors report on the development of the OMEGA EP PEPC prototype and the demonstration of high-switching contrasts exceeding 500:1 throughout the clear aperture. The key to producing this level of performance has been the reduction of stress birefringence using circular windows. In addition to the more typical role of holding the pulse in the cavity for four passes, the PEPC will be used to provide isolation from target retroreflections. Most existing multipass high-energy laser systems use frequency conversion to direct second- or third-harmonic light onto the target. This is not the case for the short-pulse part of OMEGA EP; therefore, any light reflected by the target can experience gain in the unsaturated amplifiers as it propagates back up the system, posing a significant damage threat to the system.

Additional highlights of recent research presented in this issue include the following:

- F. J. Marshall, J. P. Knauer, D. Anderson, and B. L. Schmitt present results of the absolute calibration of Kodak Biomax-MS film response to x rays in the 1.5- to 8-keV energy range. Film calibration was accomplished with an e-beam-generated x-ray source, a crystal/multilayer monochromator, a film pack, and an absolutely calibrated x-ray photon detector. The results agree with predictions from a theoretical model presented in a companion article in this issue.
- J. P. Knauer, F. J. Marshall, B. Yaakobi, D. Anderson, and B. A. Schmitt along with K. M. Chandler, S. A. Pikuz, T. A. Shelkovenko, M. D. Mitchell, and D. A. Hammer (Plasma Studies Lab, Cornell University) present a response model for Kodak Biomax-MS film to x rays. This detail film characterization starts with simple mathematical models and extends them to T-grain film. This is the companion article for the experimental results reported by F. J. Marshall *et al.* reported in this issue.
- V. Yu. Glebov, C. Stoeckl, T. C. Sangster, C. Mileham, and S. Roberts along with R. A. Lerche (LLNL) present results for a new high-yield bang time detector for the OMEGA laser. The time interval from the beginning of the laser pulse to the peak of neutron emission (bang time) is an important parameter in inertial confinement fusion experiments. The NTD streak camera currently deployed on OMEGA is saturated by neutron yields above 3×10^{13} , whereas the latest OMEGA experiments and those planned for OMEGA EP are expected to produce neutron yields above 10^{14} . This new detector will support these experiments and also high-yield experiments at the National Ignition Facility (NIF).
- C. Stoeckl, V. Yu. Glebov, P. A. Jaanimagi, J. P. Knauer, D. D. Meyerhofer, T. C. Sangster, M. Storm, S. Sublett, and W. Theobald along with M. H. Key, A. J. MacKinnon, and P. Patel (LLNL) and D. Neely and P. A. Norreys (Rutherford Appleton Laboratory) present the issues associated with operating target diagnostics in a petawatt environment. Sensitive electronic devices are difficult to operate in petawatt laser–target interaction experiments because there are copious amounts of relativistic electrons, hard x rays, and other charged particles created by the experiments. This has serious consequences for the design and integration of diagnostics inside or close to the target chamber.

- W. Guan and J. R. Marciante present simulation results for gain apodization in highly doped distributed-feedback (DFB) fiber lasers. DFB lasers can be designed with an internal grating structure to provide highly output power (up to 60 mW), single frequency, single polarization, and high optical signal-to-noise ratio. The authors investigate the effects of gain apodization on threshold behavior along with the impact on output power and mode discrimination. Apodization of the longitudinal gain profile is found to lower the laser threshold by 21% without degrading mode discrimination.

Jake Bromage
Editor

High-Contrast Plasma-Electrode Pockels Cell (PEPC)

Introduction

Many high-energy laser systems under development for inertial confinement fusion (ICF) use a multipass amplifier architecture.^{1,2} A large-aperture optical switch, which is capable of withstanding high fluence, is often utilized in these systems to control the number of passes that a laser pulse makes through the amplifier cavity. Conventional Pockels cells that use ring electrodes cannot be scaled to the large apertures required for ICF lasers. Therefore, the plasma-electrode Pockels cell (PEPC) technology, which uses high-conductivity plasmas as electrodes, was developed at Lawrence Livermore National Laboratory (LLNL) for use in ICF laser systems.³⁻⁶

Most existing multipass high-energy laser systems use frequency conversion to direct second- or third-harmonic light onto the target. This is not the case, however, for the high-energy petawatt-class laser system that is being constructed on

OMEGA EP at the Laboratory for Laser Energetics.¹ In this short-pulse system, the light is not frequency converted before being sent to the target. Any light reflected by the target can therefore experience gain as it propagates back up the system. Because the amplifiers are unsaturated, a retroreflected pulse can experience high gain, posing a significant threat of system damage. Isolation of the amplifier cavity from back-reflected light is, therefore, required on this system.

In addition to the more typical role of holding the pulse in the cavity for four passes, the OMEGA EP PEPC will be used to provide isolation from target retroreflections. This concept is illustrated in Fig. 107.1. Figure 107.1(a) shows a block diagram of a portion of the OMEGA EP Laser System; Fig. 107.1(b) is a timing diagram showing the state of the PEPC switch. The pulse from the laser sources area is injected into the beamline at the transport spatial filter (TSF) at time T and enters the

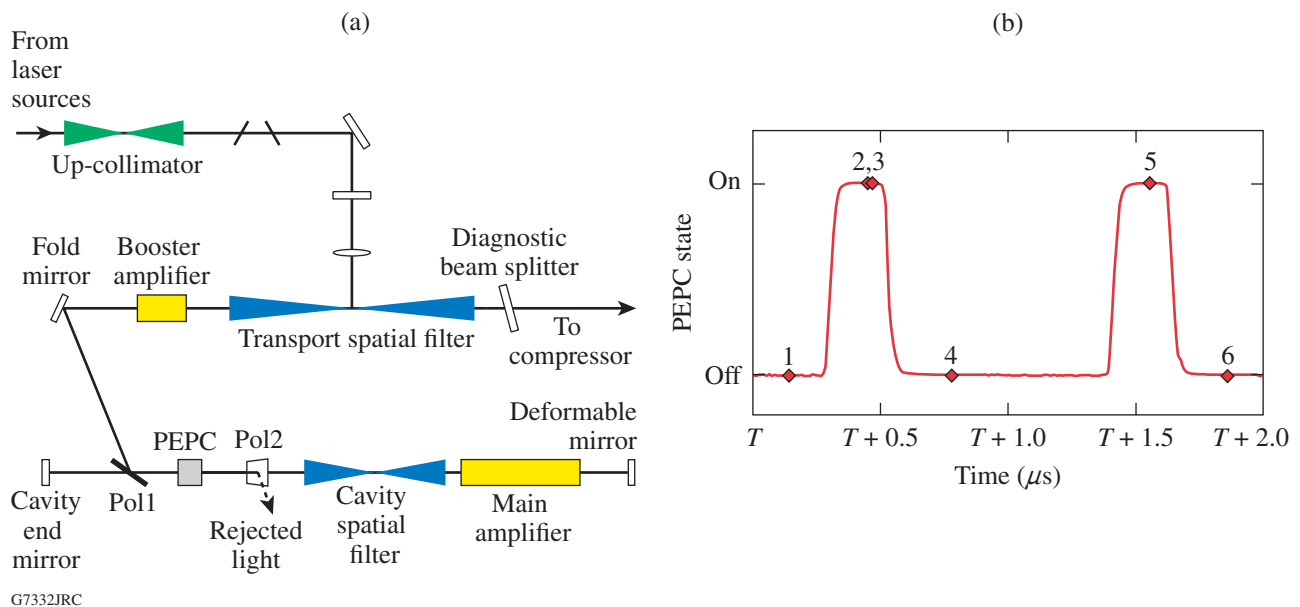


Figure 107.1 (a) Diagram of the OMEGA EP Laser System showing the PEPC in relation to key beamline components. (b) Timing diagram showing the state of the PEPC as a function of time. Times during which the laser pulse passes through the PEPC are highlighted.

amplifier cavity by reflecting from the cavity polarizer. The pulse makes Pass 1 through the PEPC while the PEPC is in its unenergized state. The pulse is amplified by two passes through the main amplifier chain before returning for Pass 2 through the PEPC, which will then be switched to its active state. This allows the laser pulse to remain in the amplifier cavity for two more passes. At Pass 4, the PEPC is again unenergized to couple the pulse out of the amplifier cavity, from which it is transported to the target chamber. Approximately 700 ns later, the retroreflected pulse couples back into the amplifier cavity for Pass 5 through the PEPC. The PEPC must be energized at this time to switch the retroreflected pulse out of the cavity to a beam dump via a polarizer labeled Pol 2 in Fig. 107.1(a). Any residual light that is not switched out of the cavity will be reamplified; therefore, the PEPC must be in the unenergized state upon its return at Pass 6 to ensure that the light is not trapped in the cavity and further amplified.

This new role of providing isolation places greater demands on the switching contrast ratio (the ratio of maximum transmission to minimum transmission of the PEPC between two ideal polarizers). To control the amplified passes through the cavity (Passes 1 through 4), the PEPC is required to provide a contrast of $>100:1$ averaged over the clear aperture, or $>50:1$ locally. To provide sufficient isolation on the OMEGA EP system for Passes 5 and 6, however, the PEPC is required to switch with a contrast ratio exceeding $500:1$ locally, i.e., at all points in the clear aperture.

This requirement exceeds the performance reported on existing PEPC cells, which are typically limited to approximately $100:1$ locally, primarily due to stress-induced birefringence in the vacuum-loaded windows.^{5,7} This article describes a redesigned PEPC that achieves a significantly higher contrast. It addresses the development of a window geometry that exhibits low stress-induced birefringence required to increase contrast and presents observations of a PEPC switching contrast ratio that reliably exceeds the $500:1$ requirement.

High-Contrast PEPC Design

The prototype PEPC cell, seen in operation in Fig. 107.2, was built to evaluate design concepts for increasing the switching contrast. A cross-sectional sketch of the system (Fig. 107.3) highlights the main features of the PEPC cell. The design was based on the LLNL PEPC in use by the National Ignition Facility (NIF) and was repackaged for use in a single-beam configuration.⁷ The main structural components, the two halves of the cell body, are made of aluminum and are anodized to provide a dielectric barrier from the plasma. Sandwiched between the cell

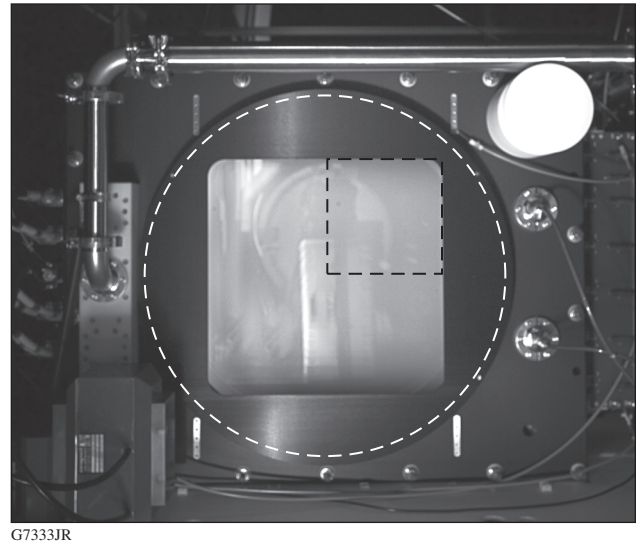


Figure 107.2

Photograph of the prototype PEPC during plasma ignition. The outline of the windows is indicated by the white dashed circle, and the region analyzed by the stress birefringence model is indicated by the black dashed square.

body halves is a glass midplane, with the electro-optic crystal potted in the center using an aerospace silicone epoxy. The electro-optic crystal is a $40 \times 40 \times 1$ -cm plate of Z-cut KDP grown via the rapid-growth method at LLNL.⁸ Fused-silica windows, which will be discussed in more detail in **Reduction of Window Stress Birefringence** (p. 131), are mounted on the cell body. These windows are circular, as indicated by the white dashed line in Fig. 107.2.

The plasma electrodes are formed in two chambers between the glass midplane and the windows. The cell is evacuated using a turbomolecular pump and back-filled with helium to 80 mT. Graphite electrodes are mounted on either end of the plasma cavity. The anodes are segmented into six button-type electrodes and the cathodes are planar magnetrons. A simmer discharge is initiated by breaking down the gas between the cathode and a nearby starter anode rod. A low-density discharge is maintained across the plasma channel for 450 ms. Near the end of the simmer discharge, a $10\text{-}\mu\text{s}$, 4-kV pulse is applied, which increases the plasma density to $>10^{12} \text{ cm}^{-3}$ to create high-conductivity electrodes.⁹ When the plasma is in this high-conductivity state, a 250-ns, 18-kV switch pulse applied between the plasmas produces the electric field necessary to impart a half-wave retardance on the 1053-nm incident beam. The electrode size produces a plasma channel that is 8 cm wider than the vertical extent of the clear aperture, thereby mitigating the effects of plasma pinching.^{10,11}

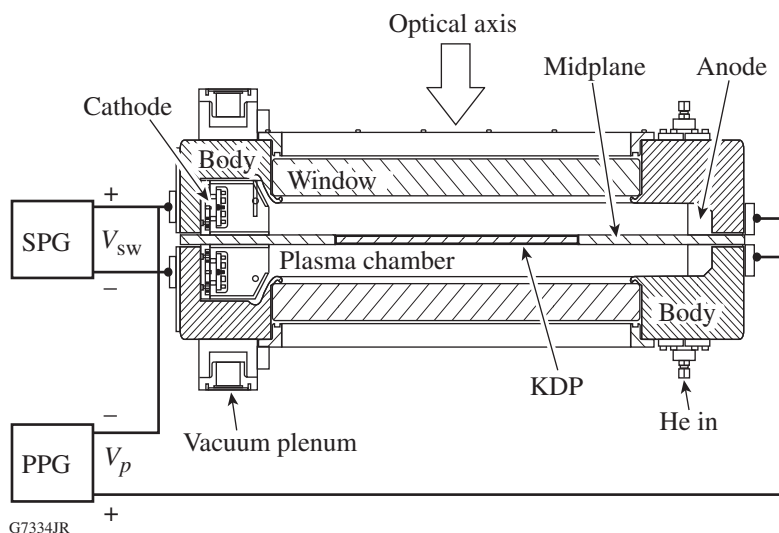


Figure 107.3

Cross-sectional view of the PEPC cell showing the key elements of the PEPC system. SPG denotes the switch pulse generator, and PPG indicates two plasma pulse generators.

Reduction of Window Stress Birefringence

The primary contrast limitation in the NIF PEPC cell design is the stress-induced birefringence in the square windows that form the air-vacuum barrier for the plasma. To achieve the contrast level required for OMEGA EP, it was necessary to understand the root cause of this birefringence. A finite-element analysis (FEA) code (ANSYS) was used to model the stress fields induced in both square windows, such as those used in the LLNL PEPC cells, and the proposed circular windows.

FEA models of the windows were generated using 20-node quadrilateral elements with a resolution in X and Y (the plane parallel with the faces of the window) equal to 10 mm and a resolution in Z equal to 1 mm. Only one quadrant of the window was modeled because of symmetry. To better simulate edge effects, a finer mesh was used near the edges of the window. Each window was assumed to be simply supported on the perimeter of the vacuum face with a uniform pressure applied to the opposite surface. The von Mises stresses were obtained from the model at every point on the sampling mesh. Because it was found that the resulting birefringence asymptotically approached a solution with decreasing step size in Z , these stresses were linearly interpolated in Z to improve the resolution through the thickness of the window.

The Wertheim stress optic law was applied to the FEA results to predict the net birefringence.¹² By modeling the birefringent window between two ideally crossed polarizers, the passive contrast could be predicted at every point. The numerical limit for the passive contrast ratio, limited by the numerical accuracy of the FEA code, was found to be approximately 5000:1. Figure 107.4 shows model predictions for both

a square $430 \times 430 \times 35$ -mm fused-silica window used in the LLNL PEPC cells and a 600-mm-diam, 40-mm-thick circular fused-silica window that was used for the LLE PEPC. In Figs. 107.4(a) and 107.4(c), 3-D maps of the magnitudes of the von Mises stresses in one quadrant of the clear aperture are shown, i.e., the region plotted in Fig. 107.4 corresponds to the black dashed square indicated in Fig. 107.2. The corresponding 2-D map of the passive contrast ratio in that same region of the square window is depicted in Fig. 107.4(b). In the case of the circular window, the calculated contrast ratio was beyond the numerical limit, and therefore no corresponding contrast ratio map is shown for this case.

The results show clearly the difference in performance between the square-window geometry and the new circular-window geometry. The model of the square window predicted a concentration of stress near the corner of the clear aperture and a resultant degradation of the contrast ratio in the corners of the clear aperture that has been reported elsewhere.^{5,7} In contrast, the calculation for the circular window reveals that the model predicted no measurable degradation of the contrast ratio for this window.

This result cannot be attributed to lower stress in the circular window because the stress in the circular window was nearly 40% higher than in the square window. However, the stress in the circular window possesses a high degree of odd symmetry, with compressive stress on the air side effectively canceling the birefringence arising from the tensile stress on the vacuum side of the window. Therefore, the net birefringence experienced by the laser pulse after propagation through the entire circular window is negligible. The stresses in the square

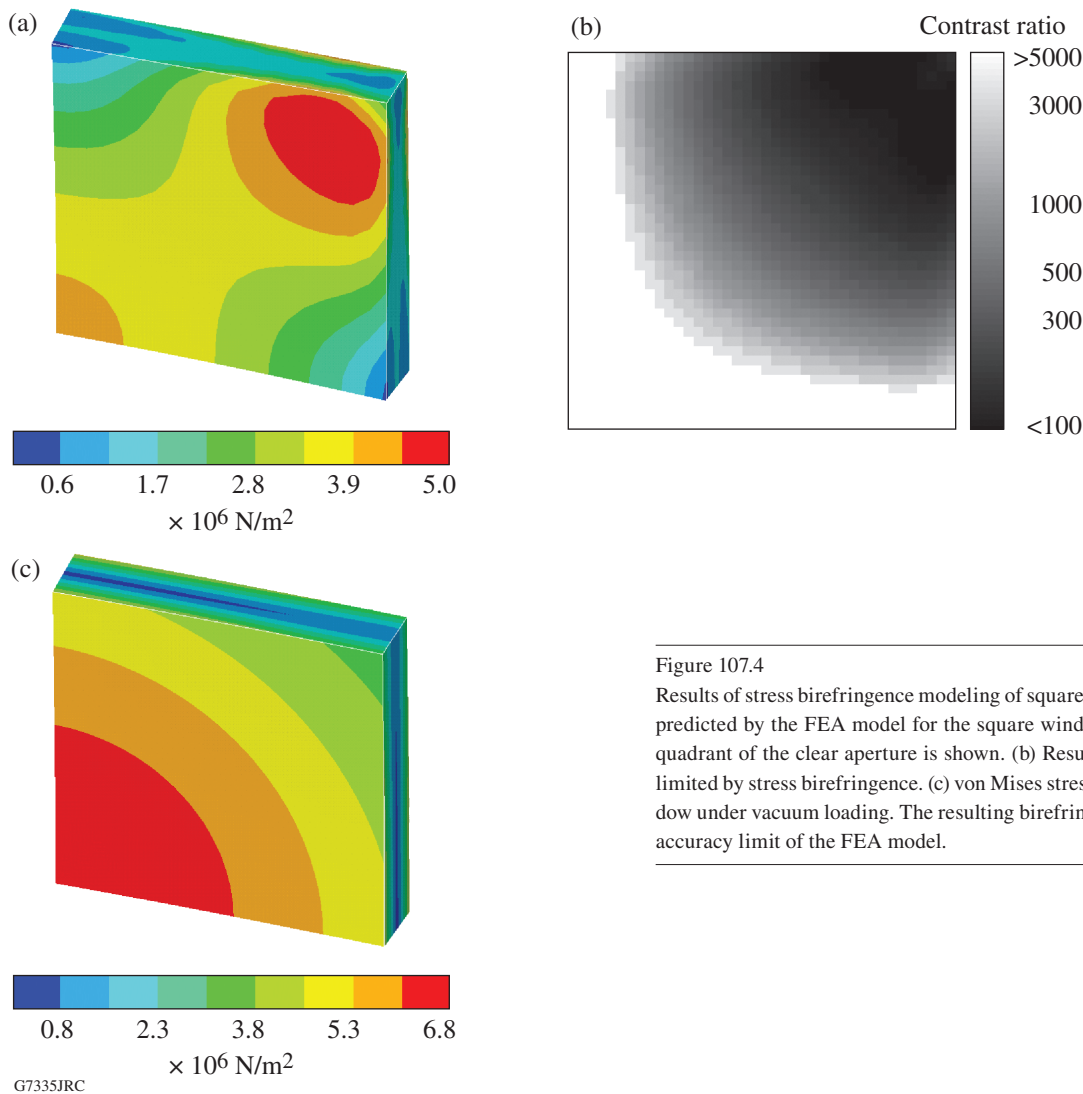


Figure 107.4

Results of stress birefringence modeling of square windows. (a) von Mises stresses predicted by the FEA model for the square window under vacuum loading. One quadrant of the clear aperture is shown. (b) Resulting predicted contrast ratio as limited by stress birefringence. (c) von Mises stresses predicted for a circular window under vacuum loading. The resulting birefringence was within the numerical accuracy limit of the FEA model.

window lack this degree of symmetry near the corners, where a significant retardation results. By the same logic, the result would not be expected to be significantly affected by the slightly higher thickness of the circular window, as was verified numerically.

Experimental Apparatus and Results

In this section, the characterization of the PEPC performance, the experimental testing apparatus, and a time-resolved polarimeter using a full-aperture beam is described, and the performance measured on the system is presented.

1. Full-Aperture Time-Resolved Polarimeter

The switching contrast of the PEPC was measured using the polarimeter system sketched in Fig. 107.5. A *Q*-switched Nd:YLF laser provided laser pulses that were sufficiently short

(<30 ns) to adequately sample the 200-ns switch pulses. The Gaussian beam was made uniform by a refractive top-hat generator, then expanded to approximately a diameter of 20 mm. A photodiode monitored the laser pulse energy and a prepolarizer fine-tuned the incident polarization to be aligned to the KDP crystal. A reflective beam expander featuring a pair of parabolic mirrors expanded the beam to a diameter of 60 cm and directed it toward the PEPC aperture.

The PEPC was mounted on a structure that allowed adjustment to the tip and tilt angles. This allowed a conoscopic alignment technique to be used to align the PEPC crystal axis to the illuminating beam.¹³ The structure also allowed horizontal translation of the entire PEPC cell and enabled measurement of the obscured region.

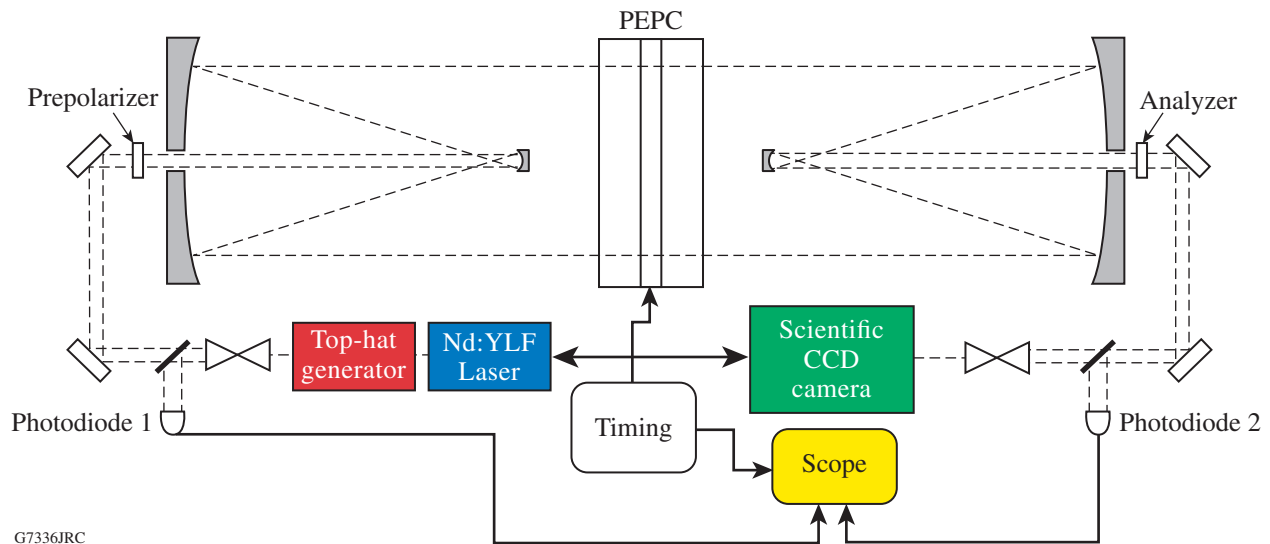


Figure 107.5
Diagram of the full-aperture polarimeter system used to test the PEPC performance.

The transmitted beam was down-collimated using an identical reflective beam expander and then passed through an analyzing polarizer. A beam sampler reflected a portion of the beam to a second photodiode. An image of the PEPC aperture was formed from the remaining beam onto a cooled 16-bit scientific CCD camera.

The laser was synchronously pulsed with the PEPC switch pulse using timing signals generated by a pulse generator. The timing system was also used to trigger an oscilloscope to capture waveform data from the photodiodes. The photodiode signals were used to measure the spatially averaged contrast over the full aperture, and the image data from the CCD camera were used to measure the contrast locally.

The contrast-ratio measurement proceeded by measuring the transmitted pulse energy with the system in a high-transmission state (or bright state) and repeating this measurement with the system in a low-transmission (dark) state. The ratio of the measurements (with background subtracted from the camera data) formed the switching contrast. To increase the dynamic range of the measurement, calibrated neutral-density filters were inserted for the bright measurements to avoid saturating the sensors while using an illumination level that would provide a measurable signal for the dark measurements. Locally, the contrast-ratio measurement is limited by the Polarcor polarizers to $>10,000:1$, with the minima occurring in two opposing corners of the clear aperture. Averaged over the full aperture,

contrast ratios exceeding $30,000:1$ can be reliably measured. Figure 107.6 shows a local contrast map produced with no PEPC cell in the system and illustrates the measurement limit of the system. The obscuration in the center of the contrast map is due to the mounts for the two secondary mirrors.

2. Passive Contrast Results

Passive contrast measurements were conducted to assess performance limits imposed by birefringence in the PEPC windows and imperfections in the KDP crystal. They were first performed with the cell at atmospheric pressure to assess any inherent birefringence caused by dislocations in the KDP crystal or by mounting-induced stress in the fused-silica windows. The resulting contrast map is shown in Fig. 107.7(a). The minimum contrast ratio in this unloaded condition was approximately $2500:1$, corresponding to a region of the window that was slightly stressed due to the window mounting. The full-aperture contrast ratio, measured using the photodiodes, was $19,800:1 \pm 1800:1$, the error range being one standard deviation. Thus, the combined effects of window-mounting stress and KDP crystal imperfections were sufficiently low to achieve a local minimum contrast ratio well in excess of $1000:1$.

The vacuum-loaded condition was then tested by evacuating the cell to below 100 mT and measuring the passive contrast in the same manner. The result of this measurement is shown in the contrast map in Fig. 107.7(b). In the vacuum-loaded condition, the minimum contrast ratio dropped only to $\sim 2000:1$ and

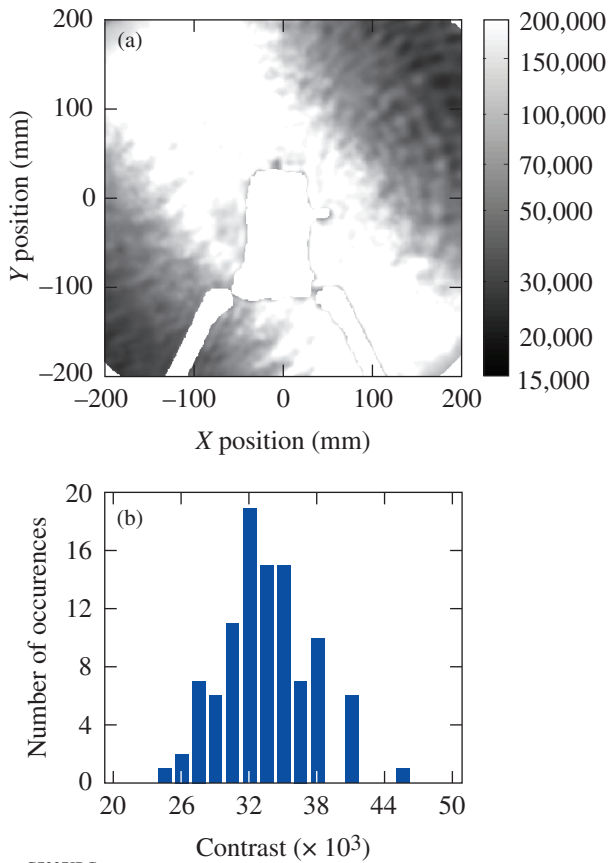


Figure 107.6

Baseline passive contrast-ratio measurements performed without the PEPC cell introduced into the polarimeter, indicating the maximum measurable contrast ratio. (a) Local contrast map obtained from image data. (b) Histogram of full-aperture contrast measurements obtained from photodiode data.

the full-aperture contrast was $20,400:1 \pm 1800:1$. Some stress birefringence is evident, leading to a somewhat suppressed contrast ratio near the corners. The birefringence is low enough, however, to allow switching contrast well in excess of our contrast ratio requirement of $>500:1$.

It should be noted that in addition to using circular windows, certain other conditions are necessary to achieve this result. One requirement is that the window must be fully supported on compliant O rings. O rings are used to provide a vacuum seal around the windows and rest inside dovetail O-ring glands in the aluminum cell body. If the cross-section diameter of the O-ring material is too small, such that the O ring fully compresses into the gland under the vacuum load, the window comes into direct contact with the aluminum cell body and local stresses are formed that severely degrade the contrast ratio. This problem was alleviated by using an O ring with a sufficient diameter to

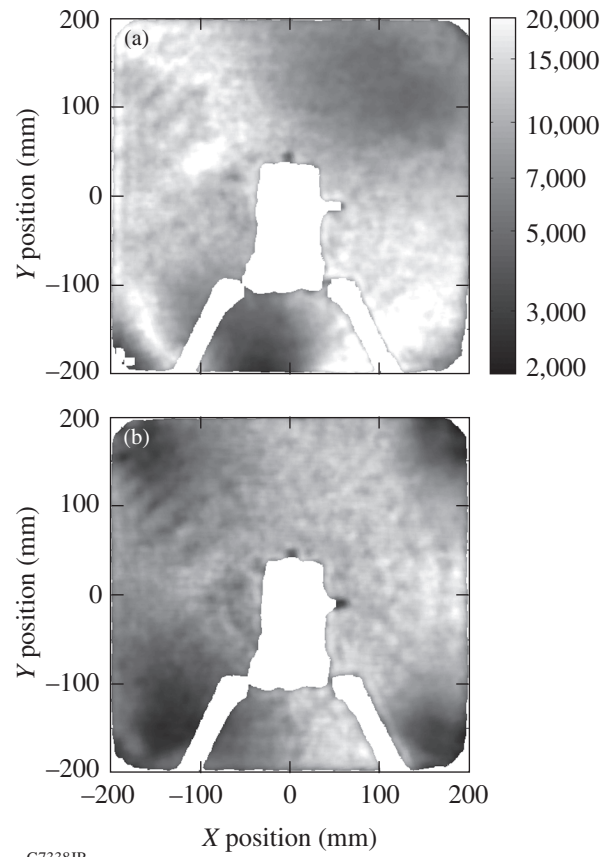


Figure 107.7

Passive contrast-ratio measurements performed with the PEPC cell in the polarimeter: (a) PEPC cell at atmosphere and (b) PEPC cell pumped down to <100 mT.

overflow the O-ring gland under vacuum loading, resulting in the window floating on top of the O ring.

3. Active Contrast Results

To assess the active-switching performance for isolating the target retroreflection at Pass 5, the prepolarizer and analyzer were aligned to each other and the laser pulse synchronized to arrive during the middle of the PEPC switch pulse [i.e., Pass 5 in Fig. 107.1(b)]. Bright-state images were obtained by setting the switch voltage to 0 V, and dark-state images were obtained with the switch voltage set to the half-wave voltage.

Figure 107.8 shows contrast results measured using this method. The surface map was generated by averaging 20 measurements acquired with the cell in three different horizontal positions. A mosaic of the three local contrast-ratio measurements was formed to minimize the obscuration from the sec-

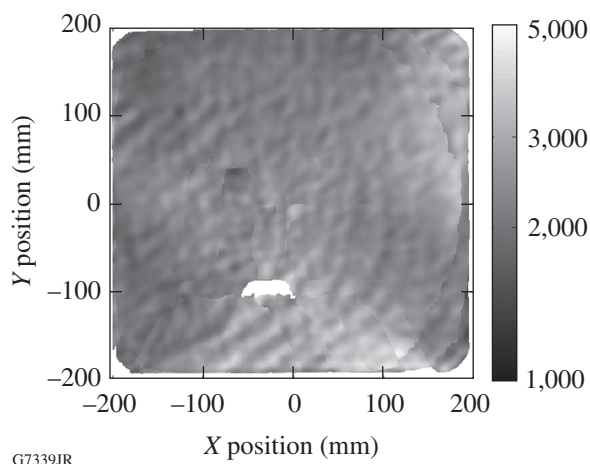


Figure 107.8

Map of the Pass-5 active contrast ratio measured over the clear aperture of the PEPC cell. The map was generated by overlapping three sequences of measurements with the PEPC cell in different positions laterally, thus minimizing the obscuration due to the secondary mirror mount.

ondary mirror mounts. The minimum contrast was 1390:1 in the averaged measurement, with the minimum occurring at the upper left-hand corner of the plot (corresponding to the top of the cathode side of the cell). Measuring the minimum contrast in each individual shot, the result was $\langle C_{\min} \rangle = 1130:1 \pm 170:1$. Both means of evaluating the results indicate that the 500:1 minimum contrast specification was comfortably exceeded. Over the full aperture, the contrast was $2280:1 \pm 150:1$ as measured with the photodiodes.

The switching contrast corresponding to Pass 6 was also measured by setting the analyzer to the crossed position with respect to the prepolarizer for the dark-state measurements. The laser pulse timing was delayed relative to the Pass-5 measurements by 300 ns, which is the propagation time of the laser pulse from the PEPC to the deformable mirror and back into the OMEGA EP beamline. This delay places the laser pulse after the falling edge of the switch pulse, as required [see Pass 6 in Fig. 107.1(b)]. Bright-state measurements were acquired by aligning the analyzer to the prepolarizer and turning the PEPC off. The local minimum for the Pass-6 switching contrast ratio was 1010:1 based on an average of 20 measurements. The single-shot minimum contrast ratio was $\langle C_{\min} \rangle = 1210:1 \pm 720:1$. The shot-to-shot variability was higher in this experiment due to variations in the overshoot at the end of the switch pulse shape. All measured shots, however, did meet the required 500:1 specification.

4. Reliability

Having demonstrated high-contrast switching performance from the PEPC, the reliability of the system was investigated. Poor contrast during a high-energy shot presents a significant risk to system safety, and thus the PEPC must meet its contrast specification reliably.

The primary cause of intermittent failures was observed to be plasma pinching, which causes a narrow region of poor switching contrast at the top or bottom of the aperture. The frequency of this occurrence was found to be strongly dependent on the operating pressure of the cell. Figure 107.9 shows the probability of a low-contrast fringe, derived from measurements of a series of 100 PEPC shots taken at various operating pressures. The probability of a low-contrast fringe decreases exponentially with pressure, becoming negligible beyond ~ 70 mT. Using a gated-image intensifier, the plasma discharge during the switch pulse was observed over the range of operating pressures shown in Fig. 107.9. At low pressures (below ~ 40 mT), the discharge was observed to occur only along a narrow strip in the clear aperture. With increasing cell pressure, the plasma spread, eventually filling the clear aperture; on the basis of this, 80 mT was selected as the standard operating pressure.

The reliability of the cell was tested by operating the PEPC for a full day and measuring the contrast throughout the day. Figure 107.10(a) shows the results of an all-day test simulating the use conditions in OMEGA EP in which the PEPC cell

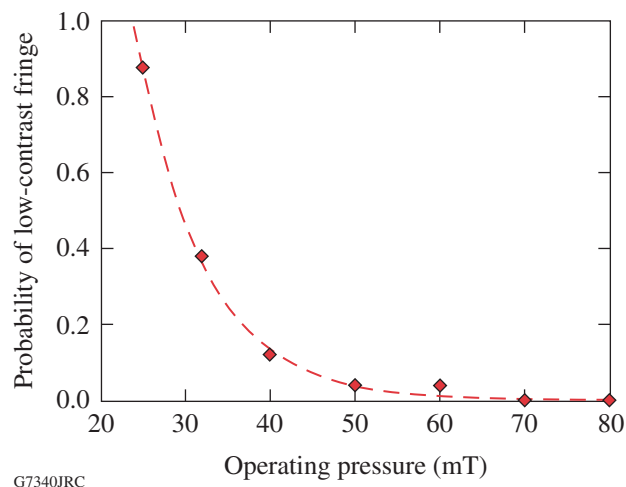


Figure 107.9

Measured probability of a low-contrast fringe occurring due to locally poor plasma conductivity, as a function of operating pressure.

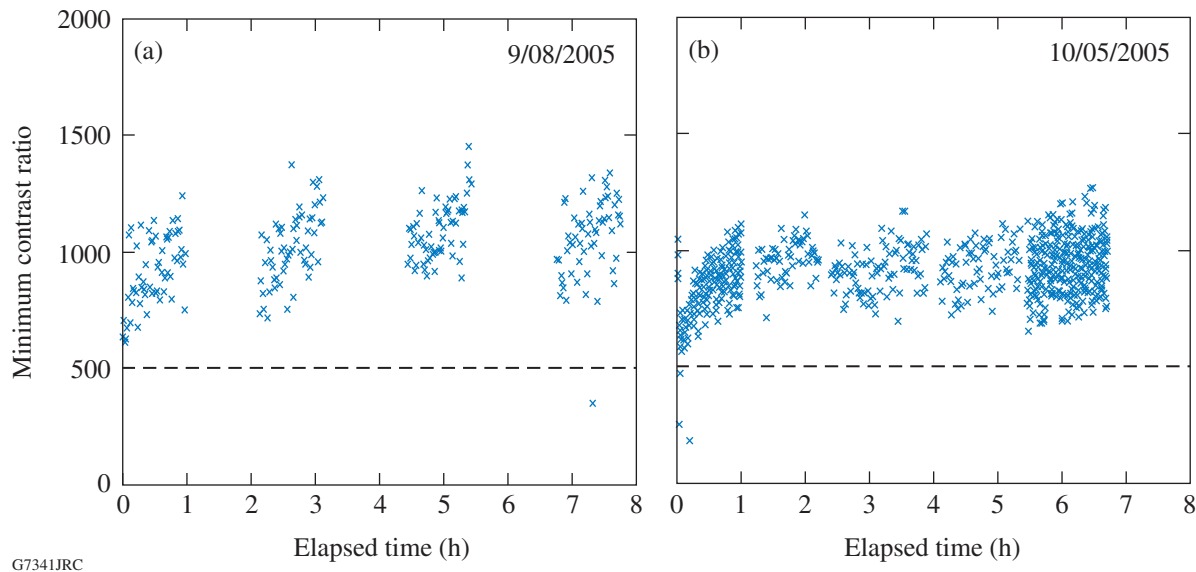


Figure 107.10

Plots of minimum local contrast ratio for individual shots during extended testing over >6 h. (a) 1-h on/off use conditions simulated and (b) PEPC run nearly continuously.

may be operated at a 1/10-Hz pulse rate for 1-h-long intervals every 2 h. In this test, the contrast was measured once per minute, although the PEPC was fired every 10 s. Of the 240 measurements that were taken during that time, one shot had a low-contrast region along the bottom edge of the clear aperture because of plasma nonuniformity. The test was repeated for continuous operation over a full day, with the results shown in Fig. 107.10(b). Images were acquired every 10 s for the first and last hours, and at 1-min intervals in between. After a 20-min warm-up period, poor shots were not observed in this test—out of over 900 measurements.

Discussion

The OMEGA EP PEPC system prototype has demonstrated that high-switching contrasts exceeding 500:1 throughout the clear aperture are obtainable using PEPC technology. The key has been the reduction of stress birefringence using circular windows. When high packing densities are required, i.e., for laser systems with a large number of closely spaced beamlines, circular windows are not feasible. This is an effective solution for systems like OMEGA EP, however, with a small number of beamlines separated by a few meters.

Work is now under way on high-contrast PEPC's for the OMEGA EP beamlines, which are currently in the integration stage. This high-contrast PEPC technology will be deployed shortly into the OMEGA EP beamlines and will provide

switching and retroreflection protection for future experimental campaigns using the laser system.

ACKNOWLEDGMENT

The authors gratefully acknowledge the contributions of Mark Rhodes, Phil Arnold, and Craig Ollis of Lawrence Livermore National Laboratories. This work was supported by the U.S. Department of Energy Office of Inertial Confinement Fusion under Cooperative Agreement No. DE-FC52-92SF19460, the University of Rochester, and the New York State Energy Research and Development Authority. The support of DOE does not constitute an endorsement by DOE of the views expressed in this article.

REFERENCES

1. L. J. Waxer, D. N. Maywar, J. H. Kelly, T. J. Kessler, B. E. Kruschwitz, S. J. Loucks, R. L. McCrory, D. D. Meyerhofer, S. F. B. Morse, C. Stoeckl, and J. D. Zuegel, *Opt. Photonics News* **16**, 30 (2005).
2. G. H. Miller, E. I. Moses, and C. R. Wuest, *Opt. Eng.* **43**, 2841 (2004).
3. J. Goldhar and M. A. Henesian, *Opt. Lett.* **9**, 73 (1984).
4. M. A. Henesian and J. Goldhar, *Opt. Lett.* **9**, 516 (1984).
5. M. A. Rhodes *et al.*, *Appl. Opt.* **34**, 5312 (1995).
6. R. Bailly-Salins, C. Sudres, and J.-P. Marret, in *Third International Conference on Solid State Lasers for Application to Inertial Confinement Fusion*, edited by H. Lowdermilk (SPIE, Bellingham, WA, 1999), Vol. 3492, pp. 148–155.

7. M. A. Rhodes, S. Fochs, and P. Bilotf, *Fusion Technol.* **32**, 1113 (1998).
8. N. P. Zaitseva *et al.*, *J. Cryst. Growth* **180**, 255 (1997).
9. C. D. Boley and M. A. Rhodes, *IEEE Trans. Plasma Sci.* **27**, 713 (1999).
10. C. D. Boley and M. A. Rhodes, in *Solid State Lasers for Application to Inertial Confinement Fusion: Second Annual International Conference*, edited by M. L. Andre (SPIE, Bellingham, WA, 1997), Vol. 3047, pp. 672–679.
11. S. N. Fochs, M. A. Rhodes, and C. D. Boley, in *Solid State Lasers for Application to Inertial Confinement Fusion: Second Annual International Conference*, edited by M. L. Andre (SPIE, Bellingham, WA, 1997), Vol. 3047, pp. 680–691.
12. M. G. Wertheim, *Comptes. Rendus Acad. Sci. Fr.* **32**, 289 (1851).
13. M. J. Guardalben, *Engineering and Laboratory Notes*, *Opt. Photonics News (Supplement)*, **8** (1997).

Absolute Calibration of Kodak Biomax-MS Film Response to X Rays in the 1.5- to 8-keV Energy Range

Introduction

X-ray film is in common use for recording the absolute x-ray fluence in high-temperature plasma experiments. The typical energy range is 1 to 10 keV, where imaging of plasma x-ray emission and spectroscopy of ionic species are often performed. Film finds use in laser-generated plasma x-ray diagnostics and in a number of related plasma-fusion-energy research fields such as in x-pinch, z-pinch, and magnetic-fusion-energy research. While directly exposed x-ray film cannot be used to time resolve the intensity of x rays, it can often be used where other means of image recording cannot.

An example of such a calibrated x-ray film is Kodak direct-exposure film (DEF).¹ DEF film was absolutely calibrated² in the 1- to 10-keV energy range. The results were fitted to a semi-empirical mathematical model of the film as described by Henke *et al.*³ and extended to DEF film,² which has two emulsion layers (one on each side). Kodak has ceased production of DEF film, and absolute calibration of a suitable replacement is needed for the eventual time when the supplies of existing DEF are exhausted. The absolute calibration of a Kodak replacement film, Biomax-MS (BMS), now in production, is the subject of this work. The measurements were taken in the x-ray laboratory at the Laboratory for Laser Energetics. Also, comparative measurements of BMS to DEF film sensitivity were taken on the OMEGA laser facility⁴ and are compared to the results of Chandler *et al.*⁵

Experimental Technique

Film calibration was accomplished with an e-beam-generated x-ray source, a crystal/multilayer monochromator, a film pack, and an absolutely calibrated x-ray photon detector. The apparatus is shown schematically in Fig. 107.11. X rays are produced in a vacuum system with the e-beam striking the desired target. The beam passes outside the vacuum system through a thin Be window (8.5 μm thick) after which the remaining path of the beam is through He gas at just over 1 atm. This minimizes beam absorption. A monochromatic beam of x rays is produced by placing a crystal or multilayer diffractor in the path of the beam with the angle of incidence equal to

the Bragg angle θ_B for the wavelength desired and the detector (film or photon counter) set to the angle $2\theta_B$. The line energies produced by this method and the corresponding monochromators and angles used to produce the monochromatic beam are given in Table 107.I.

The x-ray source intensity is measured with a liquid-nitrogen-cooled, lithium-drifted silicon Si(Li) detector⁶ read out with a pulse-height analyzer. An aperture of precisely measured dimensions (4.99 \pm 0.01 by 0.47 \pm 0.01 mm, 2.35 \pm 0.06 mm²) is placed over the entrance window of the photon detector, allowing the photon flux density to be calculated from the count rate. Since the beam is truly monochromatic, all counts above the

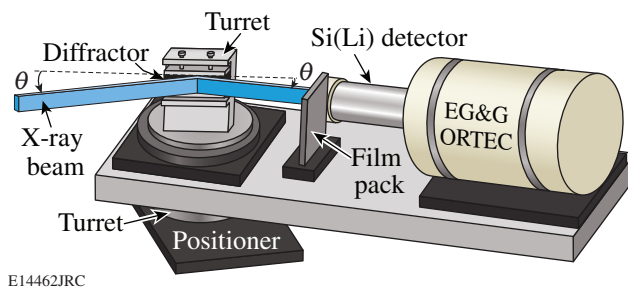


Figure 107.11
Schematic of the experimental arrangement used to calibrate Biomax-MS (BMS) film.

Table 107.I: Atomic line, line energy, monochromators, Bragg plane spacing ($2d$), and Bragg angles used for these measurements.

Line	Energy (keV)	Monochromator	$2d$ (\AA)	θ_{Bragg} ($^\circ$)
Al $K\alpha$	1.49	WB ₄ C	26.300	18.44
Ag $L\alpha$	2.98	WB ₄ C	26.300	9.10
Ti $K\alpha$	4.51	LiF(200)	4.027	43.06
Fe $K\alpha$	6.40	LiF(200)	4.027	28.76
Cu $K\alpha$	8.04	LiF(200)	4.027	22.49

noise threshold are included. Background is negligible. During film exposures, the beam intensity is measured before and at the end of the exposure. The fluence on film is determined from the average count rate and the fluence error determined from the pre- and post-exposure beam-intensity variation. Exposure times varied from as little as 2 min to as long as 3.7 h for the highest energy and density.

Film was developed by the standard method recommended by Kodak,⁷ common to both DEF and BMS. The test exposures were digitized with a calibrated PerkinElmer microdensitometer (PDS) using a 0.25-numerical-aperture (NA) lens and a $50 \times 50\text{-}\mu\text{m}$ digitizing aperture.

Absolute Measurements

A typical exposure on film is shown in Fig. 107.12(a). The exposed region of the film was limited to an image of the x-ray beam's exit aperture (nominally 1×7 mm). Figure 107.12(b) shows a lineout across the PDS digitized region. The photon detector measurements were taken in the central 0.5×5 -mm region, and the average density was inferred from a similar-sized region of the digitized density values. The horizontal gradient of the film density is due solely to the aperture, while no vertical gradient was seen in the exposures. The results of the exposures are shown in Figs. 107.13(a)–107.13(e). The DEF and BMS densities are plotted as a function of the incident fluence for the five x-ray energies used in this work [no DEF exposure was taken using Al $K\alpha$ (1.49 keV)]. The expected DEF density values determined from the Henke model² are shown with dashed lines. In general, the measured DEF density values agree well with those calculated from the model, although the

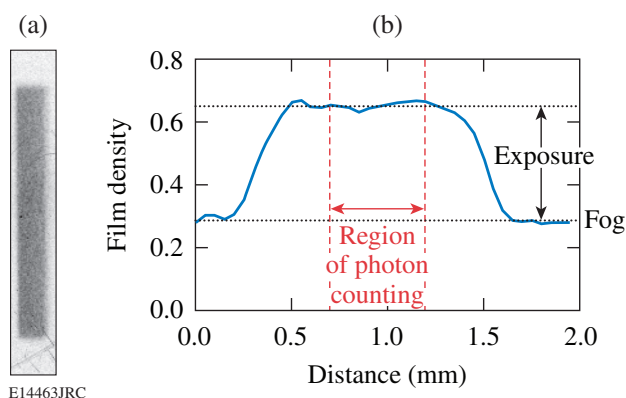


Figure 107.12

Typical exposure on (a) BMS film and (b) lineout through digitized density values. The exposure is determined by subtracting the fog level from the observed density.

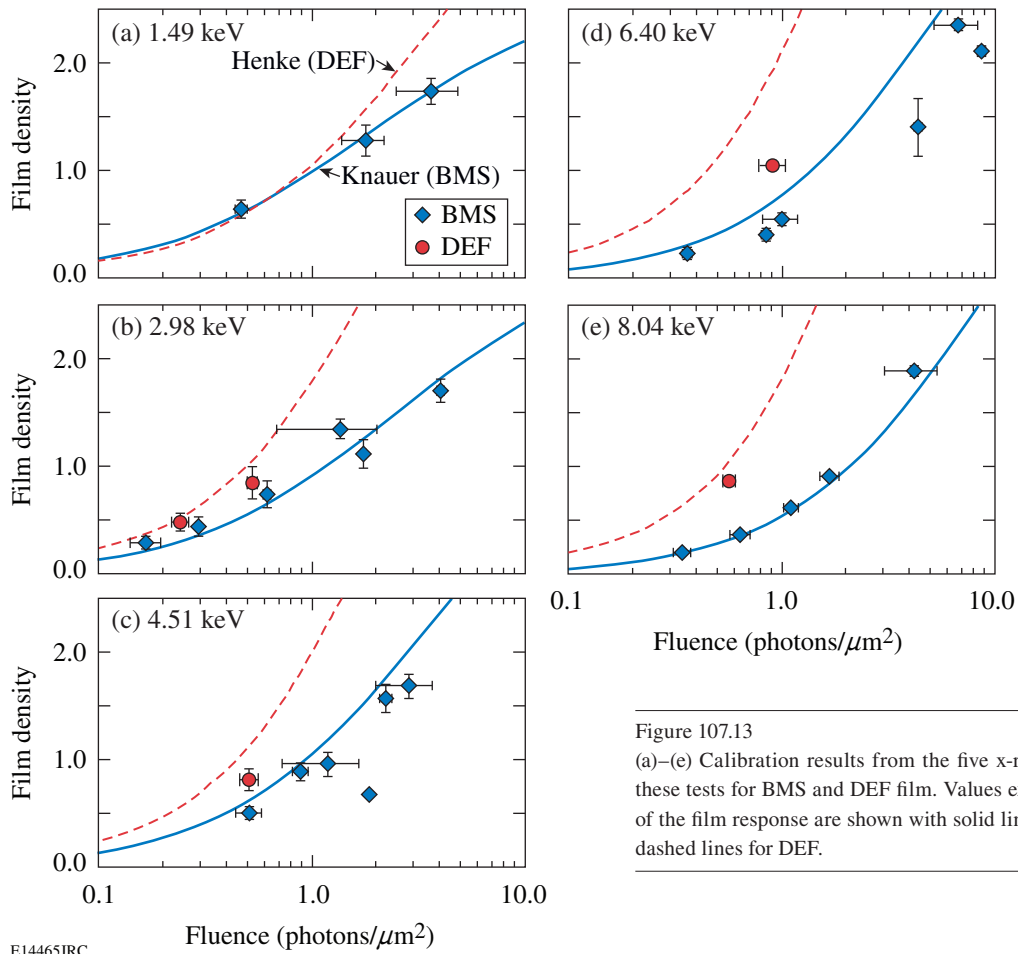
measurements are systematically lower. This is likely due to the age of the film, which has an average fog level of ~ 0.5 , considerably higher than that of fresh film (~ 0.25). This can lower the film's sensitivity.

The Henke model values are used as a basis to determine the relative sensitivity of BMS film to DEF film. At Al $K\alpha$ (1.49 keV) and Ag $L\alpha$ (2.98 keV) the sensitivities are comparable. The sensitivity of BMS drops farther compared to DEF at higher energies and is considerably lower ($\sim 2\times$ less sensitive) at the highest energy measured [Cu $K\alpha$ (8.04 keV)]. This is a consequence of the choice of emulsion (two thin emulsion layers, one on each side of the film⁸) and is expected. The BMS measured densities versus photon fluence and energy are used to determine the best-fit parameters of a mathematical model of the film response, given in a companion article in this issue (**Response Model for Kodak Biomax-MS Film to X Rays**, p. 142).⁸ The results of this model fitting are shown with solid lines in Figs. 107.13(a)–107.13(e).

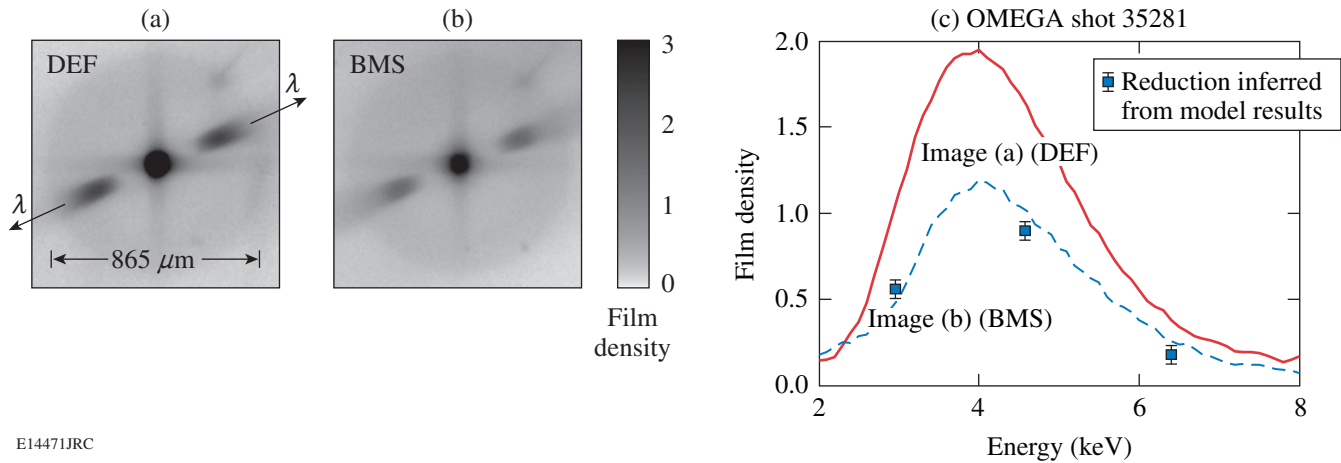
Comparative Measurements

Simultaneous measurements over the energy range from ~ 2 keV to 8 keV were obtained by placing DEF and BMS film at the image planes of two images of a four-image Kirkpatrick-Baez (KB) microscope system,⁹ which uses a transmission grating for wavelength (equivalently energy) dispersion.¹⁰ The image magnification was 20 and the wavelength dispersion was $0.586 \text{ \AA}/\text{mm}$. Figures 107.14(a) and 107.14(b) show images obtained with DEF and BMS film on an experiment performed with the 60-beam OMEGA Laser System.⁴ The laser target was a 15-atm- D_2 -filled, $27\text{-}\mu\text{m}$ -thick-plastic-shell target imploded with 23 kJ of 351-nm laser light using a 1-ns square pulse shape. The grating-dispersed emission from the intense core region is indicated with arrows on the DEF-recorded image [Fig. 107.14(a)]. The exposure levels obtained with BMS film on the same target experiment [Fig. 107.14(b)] are significantly lower. The sensitivity of the two films is compared by using the known grating dispersion of this system to determine the film density as a function of energy, and by the assumption that the two imaging systems are identical. Figure 107.14(c) shows the DEF and BMS film-density energy spectra obtained from the images shown in Figs. 107.14(a) and 107.14(b). The density obtained with BMS film is seen to be significantly less than that obtained with DEF film above ~ 3 keV.

Comparison of these results with the absolute measurements presented earlier is accomplished with the two mathematical models. The Henke *et al.*² model of DEF response [dashed lines in Figs. 107.13(a)–107.13(e)] is used to determine the



E14465JRC



E14471JRC

Figure 107.14

Comparison of DEF and BMS film response determined by two images taken with a grating-dispersed KB microscope on a single OMEGA target shot. (a) DEF-recorded image; (b) BMS-recorded image; (c) film-density/energy spectra from DEF and BMS determined from (a) and (b).

corresponding fluence, and the Knauer *et al.*⁸ model is used to calculate the values expected for BMS film. The values determined for 2.98, 4.51, and 6.40 keV are shown as data points in Fig. 107.14(c). The error bars represent uncertainty in the film-density values of ± 0.05 . The inferred density values are in close agreement with the BMS-measured film-density spectrum at all three energies. The BMS density is less than the DEF density by approximately a factor of 2 above 3 keV. Chandler *et al.*⁵ have made similar comparative measurements of DEF and BMS film using a spectrometer and x rays from an *x*-pinch source. They find an asymptotic BMS to DEF density ratio of ~ 0.55 at the high-energy limit of their measurements (3 to 6 keV). This is in good agreement with both the absolute measurements and comparative measurements presented in this work.

ACKNOWLEDGMENT

This work was supported by the U.S. Department of Energy Office of Inertial Confinement Fusion under Cooperative Agreement No. DE-FC52-92SF19460, the University of Rochester, and the New York State Energy Research and Development Authority. The support of DOE does not constitute an endorsement by DOE of the views expressed in this article.

REFERENCES

1. Kodak DEF film was manufactured by the Eastman Kodak Company, Rochester, NY 14650.
2. B. L. Henke *et al.*, *J. Opt. Soc. Am. B* **3**, 1540 (1986).
3. B. L. Henke *et al.*, *J. Opt. Soc. Am. B* **1**, 818 (1984).
4. T. R. Boehly, D. L. Brown, R. S. Craxton, R. L. Keck, J. P. Knauer, J. H. Kelly, T. J. Kessler, S. A. Kumpan, S. J. Loucks, S. A. Letzring, F. J. Marshall, R. L. McCrory, S. F. B. Morse, W. Seka, J. M. Soures, and C. P. Verdon, *Opt. Commun.* **133**, 495 (1997).
5. K. M. Chandler, S. A. Pikuz, T. A. Shelkovenko, M. D. Mitchell, D. A. Hammer, and J. P. Knauer, *Rev. Sci. Instrum.* **76**, 113111 (2005).
6. An ORTEC Poptop Si(Li) detector was used for these calibrations: Model #1019P, S/N 303-T7076 with bias set to 1000 V negative as per manufacturer's calibration instructions.
7. DEF and BMS film was developed in an auto film processor using gentle agitation as follows: 5 min in Kodak GBX developer, 30 s in stop bath, and 6 min in fixer. A post rinse in photoflo and water followed.
8. J. P. Knauer, F. J. Marshall, B. Yaakobi, D. Anderson, B. A. Schmitt, K. M. Chandler, S. A. Pikuz, T. A. Shelkovenko, M. D. Mitchell, and D. A. Hammer, presented at the 16th Annual Conference on High-Temperature Plasma Diagnostics, Williamsburg, VA, 7–11 May 2006 (Paper WP41); also this LLE Review.
9. F. J. Marshall and Q. Su, *Rev. Sci. Instrum.* **66**, 725 (1995).
10. F. J. Marshall, J. A. Delettrez, R. Epstein, and B. Yaakobi, *Phys. Rev. E* **49**, 4381 (1994).

Response Model for Kodak Biomax-MS Film to X Rays

Introduction

X-ray-sensitive film is used for a variety of imaging and spectroscopic diagnostics for high-temperature plasmas. New film becomes available as older films are phased out of production. Biomax-MS is a “T-grain” class of film that is proposed as a replacement for Kodak direct-exposure film (DEF). A model of its response to x rays is presented. Data from dimensional measurements of the film, x-ray transmission measurements, scanning electron microscope (SEM) micrograph images, and x-ray calibration are used to develop this sensitivity model of Biomax-MS film as a function of x-ray energy and angle of incidence. Relative response data provide a check of the applicability of this model to determine the x-ray flux from spectrum data. This detailed film characterization starts with simple mathematical models and extends them to T-grain-type film.

Kodak Biomax-MS film is manufactured as a double-emulsion film made with a T-grain silver halide. A schematic showing the physical layout of this film is shown in Fig. 107.15. An emulsion is coated onto both the top and bottom of a thick polyester base; the layers are assumed to be symmetric, i.e., the top emulsion layer is identical to the bottom emulsion layer. T-grain-type silver-halide grains have a large surface area but are very thin. They are best described as plates, not spheres. These plates are modeled as layers of grains suspended in a gelatin matrix. There is a protective coating of gelatin over the silver-halide gelatin structure. The bulk film parameters are the thickness of the polyester base, t_b ; thickness of the emulsion layer, T ; thickness of the overcoat, t_0 ; and volume fraction of silver-halide grains within the gelatin grain emulsion layer, V_f . Figure 107.16 shows an SEM picture of the structure of the Biomax-MS film. This is an image of a cleaved edge of the film showing the layers of thin silver-halide grains surrounded by gelatin.

Description of Model

X rays are incident on the film from the top at an angle of θ relative to the film surface, transmitted through the gelatin and base, and absorbed in the silver-halide grains in the top and

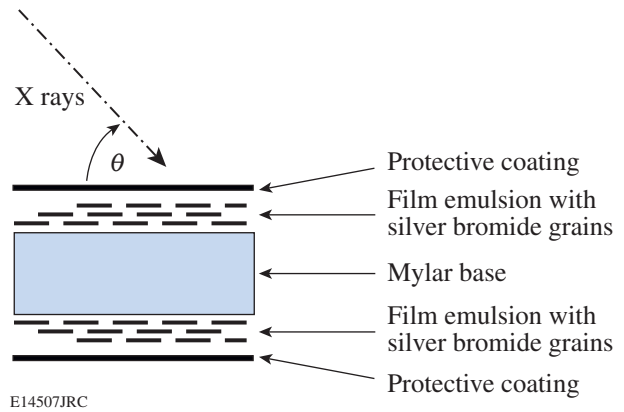


Figure 107.15

Schematic of the Biomax-MS film structure. An emulsion of grains of silver halide suspended in a gelatin is coated onto the top and bottom of a polyester base of thickness t_b .

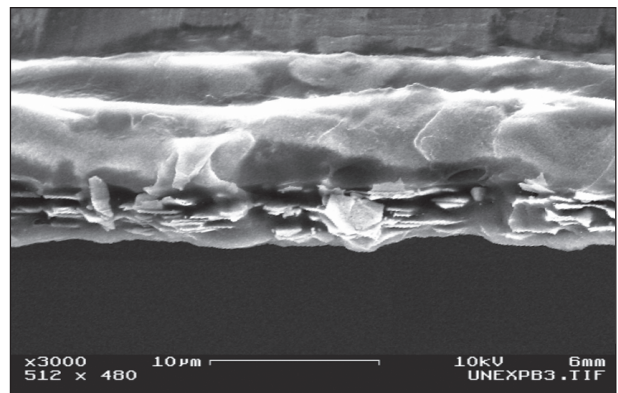


Figure 107.16

An SEM image of the edge of a cleaved edge of Biomax-MS film. The thin, layered structure of the emulsion is clearly visible within the gelatin medium.

bottom emulsion layers. The absorption of one x-ray photon is assumed to be sufficient to render that grain, and only that grain, developable. Once developed, the silver-halide grain becomes a silver structure that is opaque to light, allowing a measurement of the film's optical density. It is assumed here that the individual grain layers are independent and the total film transmission is equal to the product of each individual layer's transmission—the Nutting¹ model for optical density measurement. It has been shown to work to values of optical density near the film saturation. The silver-halide grains are modeled as being all silver bromide (AgBr) and the gelatin is modeled as $C_8H_{16}N_2O_5$. These are the same assumptions used to model the response of DEF film.²

The reader is referred to Henke *et al.*²⁻⁴ and Brown *et al.*⁵ for a detailed description of how film x-ray response is modeled. Only a brief discussion of the model and the differences required to model a T-grain film is presented in this article. Film response is defined as the relation of the recorded optical density (OD) to the incident x-ray flux (I). Reference 2 modeled the film response as $\alpha(E)OD = f[\beta(E)I]$ with the dependence of the response to the x-ray energy contained in the $\alpha(E)$ and $\beta(E)$ terms. The x-ray response model of a Biomax-MS double emulsion film is

$$\alpha OD = a \cdot \ln \left[\frac{1 + b \sin(\theta) \beta I}{1 + b \tau_e \sin(\theta) \beta I} \frac{1 + b \tau_b \tau_e \sin(\theta) \beta I}{1 + b \tau_e \tau_b \tau_e \sin(\theta) \beta I} \right] \quad (1)$$

with

$$\alpha = [\mu' / \sin(\theta)], \quad (2a)$$

$$\beta = e^{-[\mu_0 t_0 / \sin(\theta)]} \{1 - e^{-[\mu_1 d / \sin(\theta)]}\}, \quad (2b)$$

$$\tau_e = e^{-[\mu' T / \sin(\theta)]}, \quad (2c)$$

$$\tau_b = e^{-[\mu_b t_b / \sin(\theta)]}, \quad (2d)$$

and

$$\mu' = \mu_0 - \frac{1}{d} \ln \left\{ 1 - V_f [1 - e^{-(\mu_1 - \mu_0) d}] \right\}. \quad (2e)$$

Variables in Eqs. (1) and (2) with their units are defined in Table 107.II.

Table 107.II: List of variables used in modeling x-ray response of Biomax-MS film.

	Parameter	Units
θ	Angle of incidence	
μ_1	X-ray mass absorption of grain (AgBr)	μm^{-1}
μ_b	X-ray mass absorption of base (Mylar)	μm^{-1}
μ_0	X-ray mass absorption of gelatin matrix	μm^{-1}
d	Silver-halide grain thickness	μm
t_b	Base thickness	μm
T	Emulsion thickness	μm
V_f	Volume of fraction of grains	
t_0	Protective layer thickness	μm
a	Optical density constant	μm^{-1}
b	Flux constant	μm^2

Equations (1) and (2a)–(2e) form a heuristic model for the physical response of Biomax-MS film to x rays. Transmission of x rays through the emulsion layer (τ_e) and film base (τ_b) is given by Eqs. (2c) and (2d). Equation (2e) is the linear x-ray absorption coefficient (μ') for the emulsion layer. The emulsion layer is modeled as a heterogeneous mixture of AgBr and gelatin. The transmission of x rays through the protective top coat and subsequent absorption in a ArBr grain (β) are given by Eq. (2b). Reference 3 describes a methodology to determine the OD from the number of exposed grains (M) that uses the reciprocal of the exposed grain scale length, $(1/M) \times (dM/dx)$. This reciprocal scale length is given by Eq. (2a). The film response in OD calculated by using Eq. (1) has two terms in the argument of the logarithm. These terms come from the “thin-emulsion model”^{2,3} applied to the top and bottom emulsion layers, respectively.

The primary difference in this model compared to the Henke model for DEF film is the added $\sin(\theta)$ term in Eq. (2b) for the absorption of a photon in a silver-halide grain and $\sin(\theta)$ terms multiplying the x-ray flux in both the numerator and denominator of Eq. (1). These terms reflect the fact that the grains are thin plates rather than spherical: a is related to the maximum optical depth OD_s of the film and has the same dimensions as α (cm^{-1}), and b is related to the developed silver structure area with dimensions of μm^2 . Tabulated x-ray, mass absorptions,⁶ and bulk mass densities are used to compute the linear x-ray absorption coefficients [μ_{linear} (cm^{-1}) = $\mu_{\text{tabulated}}$ (cm^2/g) \times ρ_{bulk} (g/cm^3)]. In this model, $\rho_{\text{polyester}} = 1.4$ g/cm^3 , $\rho_{\text{gelatin}} = 1.4$ g/cm^3 , and $\rho_{\text{AgBr}} = 6.47$ g/cm^3 .

Determination of Model Parameters

A digital micrometer was used to measure the total thickness of the polyester base, undeveloped film, and the developed film. The micrometer faces were flat and not spherical to minimize the compression of a soft layer by the force of measurement. The polyester base was measured to be $179 \pm 1 \mu\text{m}$, the thickness of the undeveloped film was $188 \pm 1 \mu\text{m}$, and the thickness of the developed fully exposed film was $187 \pm 1 \mu\text{m}$. There is little difference between the thickness of the undeveloped film and the exposed developed film, indicating that there is only a small change in grain volume when silver halide is changed to silver. The thicknesses of the two emulsion layers and their overcoats are $9 \pm 2 \mu\text{m}$. The emulsion layer thickness T is calculated from the total emulsion thickness once the overcoat thickness t_0 is determined.

The SEM image shown in Fig. 107.16 was used to determine the silver-halide grain thickness. This image was rotated so that the grains were horizontal, and lineouts of the spatial profile across the grain images were used. Silver-halide grain thickness is defined to be the full width at half maximum of the spatial profile for each grain.

X-ray transmission data for Mn $K\alpha$, Mn $K\beta$, Cu $K\alpha$, and Cu $K\beta$ were acquired to determine the volume fraction of silver-halide grains in the emulsion layer. First, the digital micrometer data were checked by calculating the polyester base thickness needed to match the measured x-ray transmission. The base thickness calculated from these data is $180 \pm 5 \mu\text{m}$. This is in

good agreement with the micrometer measurement. X-ray transmission through the emulsion layer can be shown to be proportional to the product of the volume fraction times the emulsion thickness $V_f \times T$, $1.3 \pm 0.4 \mu\text{m}$. V_f is then calculated once T is known.

The remaining parameters a , b , and t_0 are determined by fitting the model for optical density to the x-ray exposure data and minimizing χ^2 . The absorption of higher-energy x rays (Ti $K\alpha$, Fe $K\alpha$, and Cu $K\alpha$) is low in the overcoat and, thus, insensitive to t_0 . The model formula was used to determine the constants a and b from the measured sensitivity by doing a nonlinear minimization of the calculated χ^2 of the high-energy x-ray data. A nonlinear minimum χ^2 fit for the low energy (Al $K\alpha$ and Ag $L\alpha$) was then used to determine t_0 since the low-energy x rays are more affected by the overcoat. The developing process used and the densitometer measurement of the film are described in a companion paper by Marshall *et al.*⁷ Biomax-MS film parameters determined by the above methodology are listed in Table 107.III along with the corresponding values for DEF from Ref. 2.

This model was used to calculate the x-ray flux in photons/ μm^2 to give an exposure in optical density of 0.5, 1.0, and 2.0 for Biomax-MS film as a function of x-ray energy from 1.0 to 10.0 keV. The Henke model was used to calculate the same information for DEF film. In general, the Biomax-MS film is less sensitive, i.e., requires more photons/ μm^2 for the same optical density than DEF film. Biomax-MS sensitivity is

Table 107.III: List of values, errors, and method of determination for Biomax-MS film parameters. DEF values for comparison are taken from Ref. 2.

	Biomax-MS	DEF
<i>Micrometer data</i>		
Base thickness (t_b)	$179 \pm 1 \mu\text{m}$	$185 \mu\text{m}$
Emulsion thickness (T)	$4 \pm 1 \mu\text{m}$	$13 \mu\text{m}$
<i>SEM data</i>		
Grain thickness (d)	$0.12 \pm 0.03 \mu\text{m}$	$1.6 \mu\text{m}$
<i>X-ray transmission data</i>		
Volume fraction of grains (V_f)	0.34 ± 0.08	0.4
<i>Calibration data</i>		
Protective layer thickness (t_0)	$0.4 \pm 0.1 \mu\text{m}$	$1 \mu\text{m}$
Optical density constant (a)	$0.58 \pm 0.01 \mu\text{m}^{-1}$	$0.68 \mu\text{m}^{-1}$
Flux constant (b)	$12.4 \pm 0.3 \mu\text{m}^2$	$1.69 \mu\text{m}^2$

equal to or somewhat greater than that of DEF only for x-ray energies <2 keV and for optical densities <2.0 . This confirms measurements previously reported by Chandler *et al.*⁸ on the comparison of Biomax-MS to DEF sensitivity.

Marshall *et al.*⁷ reported in a companion paper on the comparison of the response of Biomax-MS to that of DEF for spectrally dispersed data recorded with a transmission grating in a KB microscope. These data were converted to x-ray intensity versus energy with the model described in this article and the Henke model for DEF. The results are plotted in Fig. 107.17, where the maximum optical density recorded on DEF was ~ 1.8 and the maximum for Biomax-MS ~ 1.0 . The calculated x-ray flux from the DEF exposure agrees very well with the x-ray flux calculated from the Biomax-MS exposure. The incident angle of the x rays onto the film for these data was $\sim 90^\circ$.

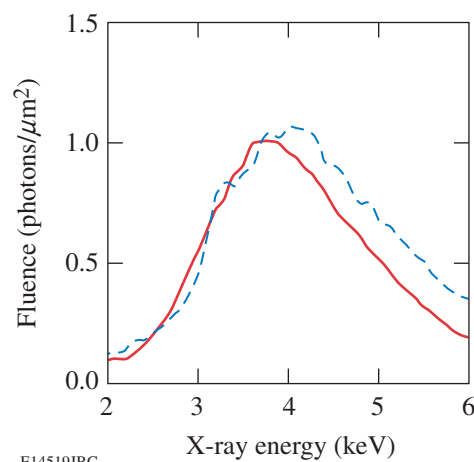
Relative sensitivity data were also recorded for x rays in a Rowland circle crystal spectrometer. A flat crystal was used to record the x-ray spectrum from an OMEGA shot from 2 to 6 keV. The x rays were recorded with an incident angle of $\sim 50^\circ$. Again, the models for DEF and Biomax-MS were used to convert the film optical density to x-ray flux. The results shown in Fig. 107.18 indicate that calculated x-ray fluxes agree to 20% for the DEF and Biomax-MS data.

Conclusions

The x-ray flux calculated from DEF using the model of Henke *et al.*² and from Biomax-MS using this model are generally in agreement. The emulsion layer is thinner for Biomax-MS than it is for DEF; therefore, the absorption of higher-energy x rays is less in the Biomax-MS film than in the DEF film. This is reflected in the significantly reduced sensitivity for Biomax-MS when compared to DEF at x-ray energies >4 keV. The grain geometries are also very different: the DEF grains are typically spherical, while the Biomax-MS grains are flat plates with a large surface area and small thickness.

ACKNOWLEDGMENT

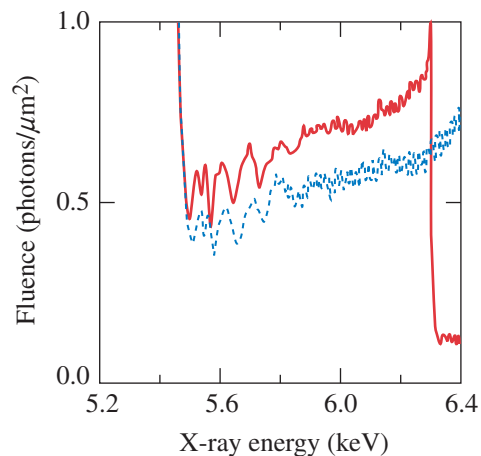
This work was supported by the U.S. Department of Energy Office of Inertial Confinement Fusion under Cooperative Agreement No. DE-FC52-92SF19460, the University of Rochester, and the New York State Energy Research and Development Authority. The support of DOE does not constitute an endorsement by DOE of the views expressed in this article.



E14519JRC

Figure 107.17

Comparison of the x-ray fluence calculated from KB microscope-dispersed spectra. The calculated DEF x-ray fluence is plotted as a solid line, and the calculated Biomax-MS x-ray fluence is plotted as a dashed line.



E14522JRC

Figure 107.18

X-ray fluence calculated for a Rowland circle spectrometer for both DEF and Biomax-MS films. The solid curve is the x-ray fluence versus energy calculated from DEF film, and the dashed curve is calculated from the Biomax-MS film.

REFERENCES

1. J. C. Dainty and R. Shaw, *Image Science: Principles, Analysis and Evaluation of Photographic-Type Imaging Processes* (Academic Press, London, 1974), p. 39.
2. B. L. Henke *et al.*, *J. Opt. Soc. Am. B* **3**, 1540 (1986).
3. B. L. Henke *et al.*, *J. Opt. Soc. Am. B* **1**, 818 (1984).
4. B. L. Henke *et al.*, *J. Opt. Soc. Am. B* **1**, 828 (1984).
5. D. B. Brown, J. W. Criss, and L. S. Birks, *J. Appl. Phys.* **47**, 3722 (1976).
6. B. L. Henke, E. M. Gullikson, and J. C. Davis, *At. Data Nucl. Data Tables* **54**, 181 (1993).
7. F. J. Marshall, J. P. Knauer, D. Anderson, and B. A. Schmitt, presented at the 16th Annual Conference on High-Temperature Plasma Diagnostics, Williamsburg, VA, 7–11 May 2006 (Paper WP40).
8. K. M. Chandler, S. A. Pikuz, T. A. Shelkovenko, M. D. Mitchell, D. A. Hammer, and J. P. Knauer, *Rev. Sci. Instrum.* **76**, 113111 (2005).

High-Yield Bang Time Detector for the OMEGA Laser

Introduction

The time interval from the beginning of the laser pulse to the peak of neutron emission (bang time) is an important parameter in inertial confinement fusion (ICF)¹ experiments. The neutron bang time is very sensitive to energy absorption and the subsequent hydrodynamic response of the target and can be directly compared with numerical simulation. Several detectors^{2–4} that have been developed to measure the neutron bang time in ICF experiments include a fast (<25-ps) streak-camera-based neutron temporal diagnostic (NTD).⁵ An NTD is currently installed on the OMEGA laser⁶ at LLE. The NTD streak camera, located at about 3 m from the target, is saturated by neutron yields above 3×10^{13} . OMEGA has produced yields of 10^{14} (Ref. 7), and fast-ignition experiments currently planned⁸ at the OMEGA Laser Facility are expected to produce neutron yields above 10^{14} . A new high-yield neutron bang time (HYNBT) detector has been developed at LLE to measure the bang time in these very high yield experiments. The HYNBT has also been developed as a prototype neutron bang time detector for high neutron yields at the National Ignition Facility (NIF). The present work is a continuation of the NIF prototype development published earlier.⁹

HYNBT Design and Setup

The HYNBT detector design, shown in Fig. 107.19, consists of three chemical-vapor-deposition (CVD) diamond detectors of different sizes and sensitivities placed in a lead-shielded housing. The HYNBT uses commercially purchased¹⁰ “optical-quality” polycrystalline DIAFILM CVD wafers. The HYNBT wafers are disks with the following dimensions: 10-mm diameter, 0.5 mm thick (Ch1); 5-mm diameter, 0.25 mm thick (Ch2); and 2-mm diameter, 0.5 mm thick (Ch3). On each side of the CVD wafer 10 nm of Cr and 50 nm of Au were deposited to provide electrical contact. Each CVD wafer was assembled in an individual aluminum housing with an SMA connector. Figure 107.20 shows the Ch3 housing before and after assembly. Each detector was pre-tested, and the three channels were assembled in a stainless steel cylinder. Figure 107.21 shows the HYNBT before and after assembly. The thin-walled

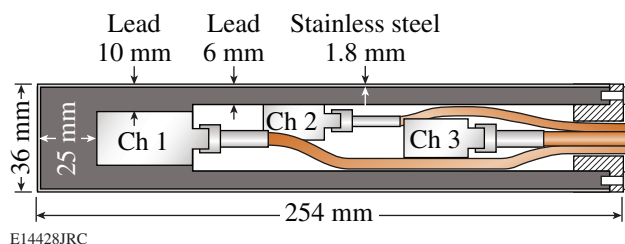


Figure 107.19
Design of the HYNBT detector.

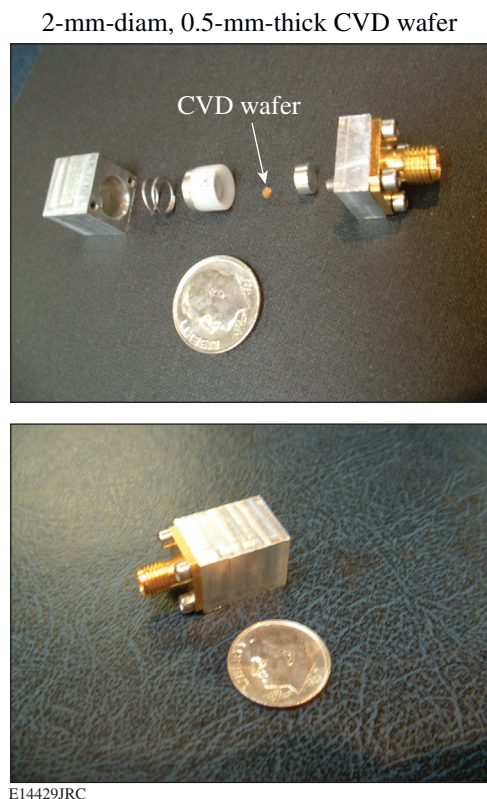


Figure 107.20
The HYNBT Ch3 housing before and after assembly.

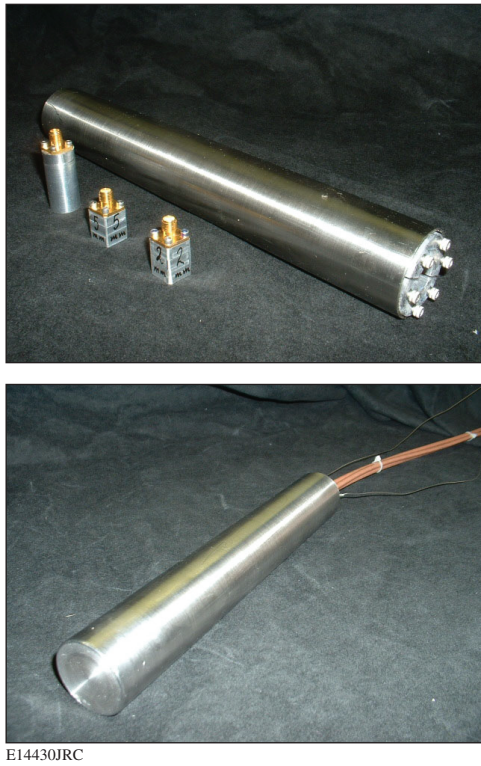


Figure 107.21
The HYNBT before and after final assembly.

stainless steel cylinder acts as a Faraday cage decreasing the electromagnetic pulse (EMP) noise. Lead shielding inside the steel cylinder protects the CVD diamond detectors from hard x rays. This shielding is not necessary for current experiments on OMEGA and was installed in anticipation of hard x rays produced by the interaction of the short laser pulse with the gold cone or shell in fast-ignition experiments.⁸ RG-142 coaxial cables are used because of their double-braid shielding design and low sensitivity to neutrons.¹¹ The 3-m-long, RG-142 cables are connected to 22-m-long, LMR-400 cables. Inside the OMEGA Target Bay, the cables are routed radially with respect to the target chamber center to minimize the interaction of neutrons with the cables. The bandwidth of the LMR-400 cables is higher than that of the RG-142 cables, but they are much more sensitive to neutrons.¹¹ This two-cable solution is a compromise between bandwidth and neutron-induced background signals. The HYNBT is deployed in the same re-entrant tube as LLE's NBT,⁴ 50 cm from the target chamber center. All of the HYNBT channels were biased at 750 V using a bias-tee (Picosecond Pulse Labs, model 5531). The signals from the HYNBT CVD diamond detectors were recorded on three channels of a 3-GHz, 10-GS/s, Tektronix TDS-694 oscilloscope. The OMEGA optical fiducial pulse

train is recorded on the fourth channel, using a fast photodiode to provide a time reference to the laser. The fiducial analysis and fitting procedure are described in Ref. 4.

HYNBT Performance

The HYNBT was tested on OMEGA with both DT and D₂ implosions. Figure 107.22 shows typical oscilloscope traces of the three HYNBT channels for a shot yielding 4.4×10^{12} DT neutrons. The measured signals were fit by a convolution of a Gaussian and an exponential decay, as described in Ref. 4. The parameter of the exponential decay represents the collection time of the carriers in the CVD diamond wafer. At a constant bias voltage, the decay parameter depends on the thickness and diameter of the CVD wafer. The optimum decay parameter for

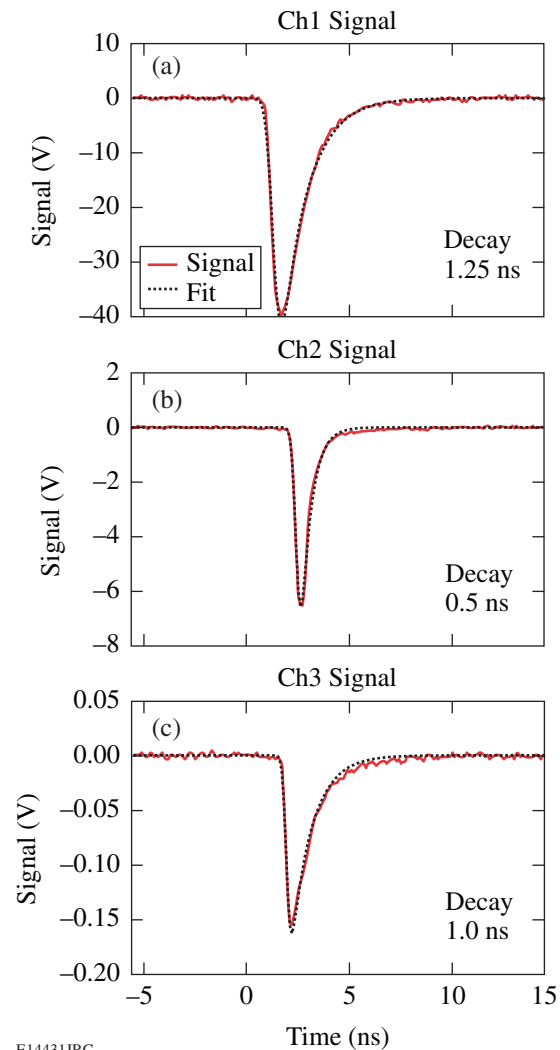


Figure 107.22
The HYNBT signal for shot 42120 with a DT neutron yield of 4.4×10^{12} .

each HYNBT channel was determined from the fit of a large number of the shots for each channel (low noise, not saturated) and was fixed for the timing analysis of all shots. The Gaussian fit parameters are free parameters for every shot to account for different yields, bang times, ion temperatures, and trigger shifts. The neutron pulse's arrival time is defined to be the center of the Gaussian portion of the fit. Figure 107.23 shows the signal amplitude of three HYNBT channels as a function of DT neutron yield. The straight lines are linear fits to the data for each channel. The first HYNBT channel saturates above a 100-V signal, and the second channel saturates above 80 V. At a yield of 1×10^{15} , the third channel will have a signal of ~ 20 V and will not be saturated. The three HYNBT channels can measure the neutron bang time in DT implosions over the yield range from 1×10^{10} to 1×10^{15} .

The timing accuracy of the HYNBT was studied by measuring the time differences among channels. Figure 107.24(a) shows the time difference between two HYNBT channels recorded on multiple shots over two shot days in May 2005. The DT yields varied from 8.4×10^{12} to 3.5×10^{13} . The rms of the time difference between these two channels is 13 ps. The HYNBT was tested five times during 2005. Figure 107.24(b) shows the time difference between the HYNBT channels appropriate for the neutron yield range during the tests. In November 2005, Ch2 of the HYNBT was used to test a gamma bang time (GBT) detector based on an optical light pipe concept;¹² the time difference between the HYNBT and the GBT had an rms of 15 ps. In all cases the internal time resolution of the HYNBT was better than 20 ps.

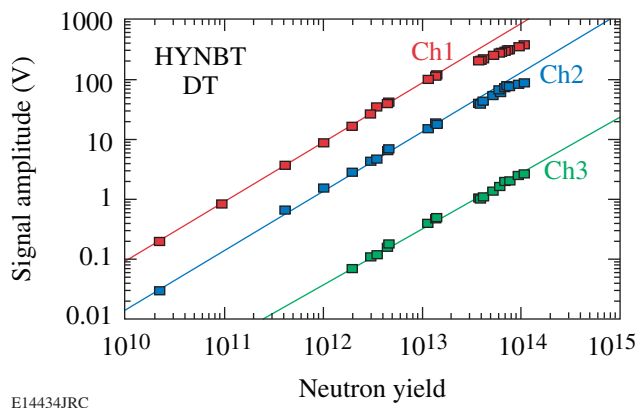
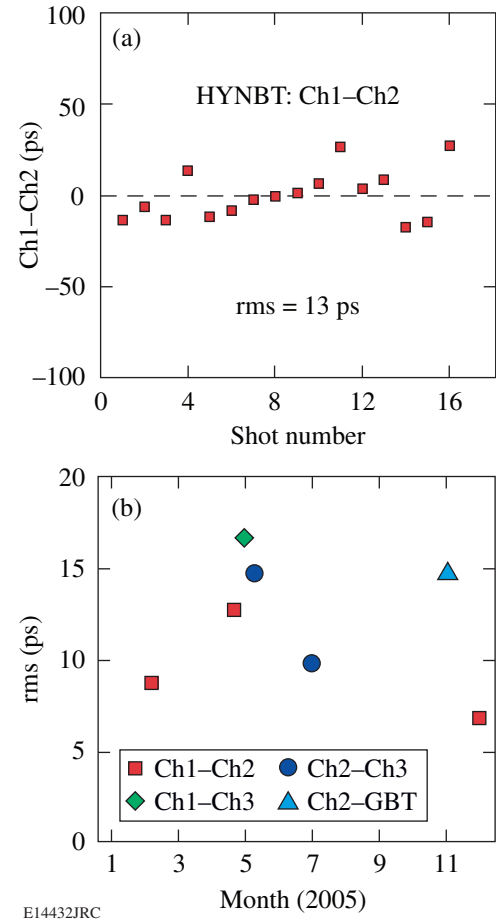


Figure 107.23
Signal amplitudes of the HYNBT channels.



E14432JRC

Figure 107.24
(a) Time difference between HYNBT Ch1 and Ch2 in May 2005; (b) rms of time differences between the HYNBT channels in 2005.

The timing calibration of the HYNBT bang time relative to the OMEGA laser pulse was established by cross-calibration against the NTD.⁵ Figure 107.25 shows the cross-calibration of the HYNBT channels and the NTD performed in December 2005, with DT yields varying from 3.0×10^{12} to 1.4×10^{13} . A good correlation between the NTD and the HYNBT is observed with an rms difference of 40 ps. This is larger than the 28-ps rms expected for the difference between two independent measurements, each with a time precision of 20 ps. The discrepancy is explained by direct neutron hits on the NTD, charged-coupled-device (CCD) camera that reduces its temporal resolution.

Although the HYNBT was designed to measure DT neutron bang time, it can also measure bang time in high-yield D_2 shots on OMEGA. Since CVD diamond detectors are less sensitive to D_2 than to DT neutrons, only the first HYNBT channel

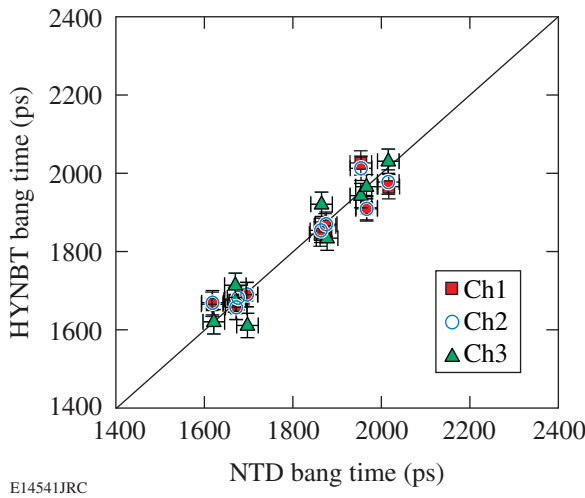


Figure 107.25
Timing cross-calibration between the HYNBT and the NTD for DT implosions. A line of equal bang times for both instruments is shown for comparison.

is sufficiently sensitive for D_2 implosions on OMEGA. Figure 107.26 shows oscilloscope traces of the first HYNBT channel for shots yielding 1.1×10^{10} and 9.3×10^{10} . At a D_2 yield of 1×10^{10} the signal amplitude is only 10 mV and is affected by EMP and digital noise since the minimum scale setting of the TDS-694 oscilloscope is 10 mV/div. Figure 107.27 shows the first-channel signal amplitude as a function of D_2 yield, and Fig. 107.28 shows the cross-calibration against the NTD. To minimize the influence of noise on the cross-calibration timing, only shots with yields above 3×10^{10} were included. With ~ 50 -ps rms, the D_2 cross-calibration is not as accurate as the DT cross-calibration because most of the signal amplitudes in Fig. 107.28 were below 100 mV.

EMP mitigation techniques used with the HYNBT design reduced the EMP noise to a level about $10\times$ smaller than that measured with LLE's NBT.⁴ Figure 107.29 shows the EMP noise levels in the least-sensitive Ch3 for different shot conditions. Figure 107.29(a) shows less-than-2-mV noise levels for the standard direct-drive shot. Figure 107.29(b) shows the EMP noise level for a direct-drive shot with backlighting. Backlighting produced additional EMP noise, and for these shot types, the noise level is below 4 mV. The indirect-drive shot with a scale-5/8 hohlraum is shown in Fig. 107.29(c) with the EMP noise below 4 mV. For all shots on OMEGA the EMP noise level in the HYNBT is below 4 mV.

Due to the lead shielding, the HYNBT is insensitive to hard-x-ray signals in direct-drive and most typical indirect-

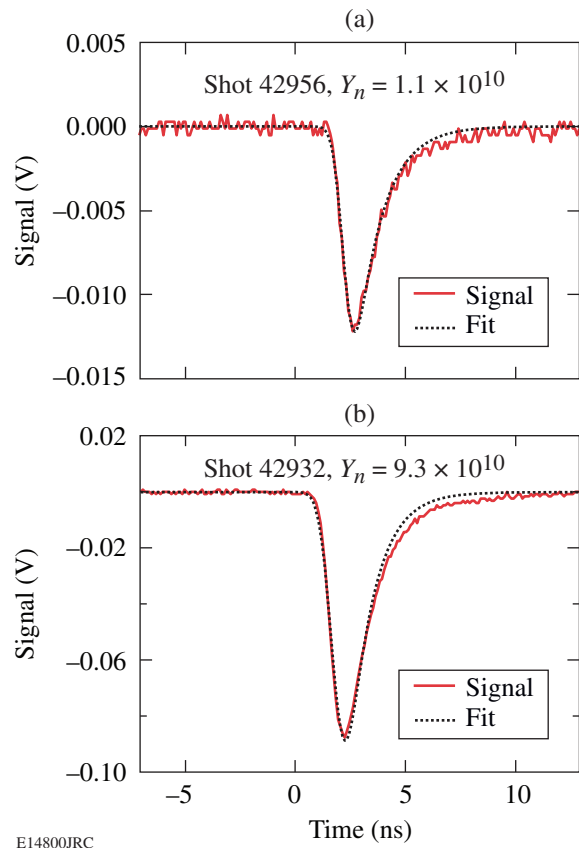


Figure 107.26
The oscilloscope traces of the first HYNBT channel for D_2 shots: (a) shot 42956 with a yield of 1.1×10^{10} ; (b) shot 42932 with a yield of 9.3×10^{10} .

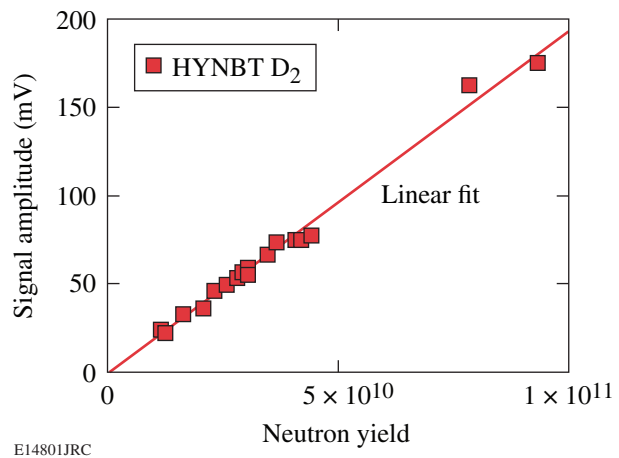
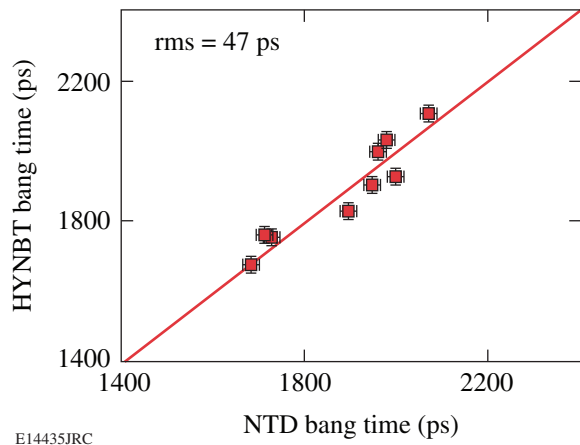


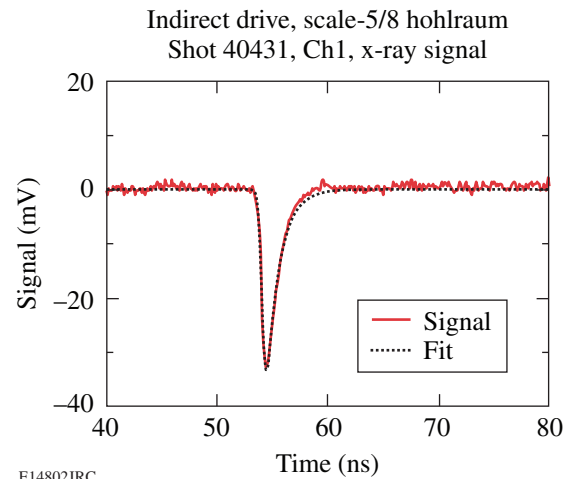
Figure 107.27
The HYNBT first-channel signal amplitude as a function of D_2 yield.



E14435JRC

Figure 107.28

Timing cross-calibration between the HYNBT first channel and the NTD for D_2 implosions. A line of equal bang time for both instruments is shown for comparison.



E14802JRC

Figure 107.30

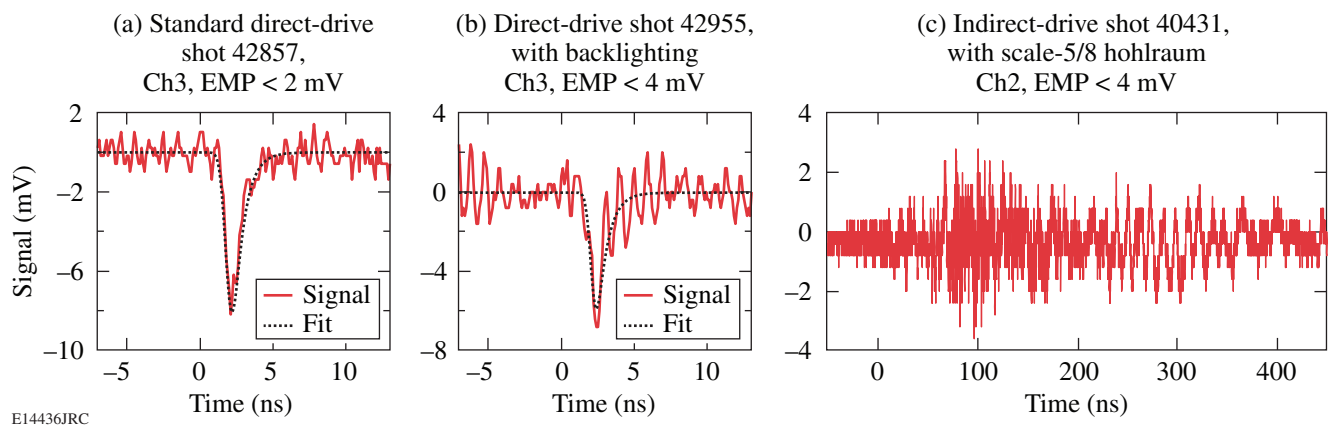
X-ray signal from the scale-5/8-hohlraum, indirect-drive shot 40433 on the HYNBT first channel.

drive shots. Only the most sensitive HYNBT channel was able to record a 30-mV x-ray signal from a scale-5/8 hohlraum, indirect-drive shot that produces $\sim 100\times$ more hard x rays than direct-drive shots (shown in Fig. 107.30). This relatively low signal is temporally separated from the neutron signal and will not compromise the HYNBT bang time.

HYNBT on the NIF

The HYNBT was also developed as a prototype neutron bang time detector for the NIF. This is a continuation of earlier work⁹ on a NIF bang time prototype. Since publication of this earlier work, the design requirements have changed: Instead of

a low-to-moderate-yield, general-purpose diagnostic, the NIF NBT detector is now required for moderate-to-high yields in the pre-ignition and early-ignition campaigns. At these yields, the original scintillator and photomultiplier channel described in Ref. 9 cannot be used. The NIF NBT is virtually identical to the OMEGA HYNBT with three or four CVD diamond channels. This design will make the NIF NBT more compact, simpler, and less expensive than an NBT employing a photomultiplier. It will be located about 40 to 60 cm from the target in a diagnostic insertion manipulator, together with other NIF diagnostics. In contrast to the OMEGA HYNBT, the shielding on the front of the NIF NBT (facing the target) will be remov-



E14436JRC

Figure 107.29

EMP noise in HYNBT Ch3 for different shots conditions: (a) standard direct-drive shot 42857; (b) direct-drive shot 42955 with backlighting; and (c) indirect-drive shot 40431 with a scale-5/8 hohlraum.

able so that x rays can be used for temporal calibration.⁹ The calibration will use x-ray emission from a gold target irradiated by a short laser pulse. The distance from the target, x-ray shielding, and cable length of the HYNBT on OMEGA are comparable to those required on the NIF. The sensitivity of the NIF NBT channels will be comparable to the corresponding HYNBT channels. The dynamic range of the NIF NBT can be increased by increasing the sensitivity of the first channel, decreasing the sensitivity of the third channel, and adding an even less sensitive fourth channel. The first-channel CVD wafer can be changed from a 10-mm-diam, 0.5-mm-thick CVD wafer to a 10-mm-diam, 1-mm-thick CVD wafer. This will increase the sensitivity by a factor of 2, which corresponds to yields of 2.5×10^{10} in D_2 and 5×10^9 in DT implosions. If NIF NBT operation will be required at lower yields, the detector can be moved closer to the target. The fourth, least-sensitive channel can be made from a smaller and thinner CVD wafer, from a neutron-hardened CVD wafer, or from a CVD wafer with impurities. All of these factors decrease the sensitivity of the CVD diamonds and shorten the temporal response. The maximum operational yield of the NIF NBT will not be determined by CVD diamond saturation but by neutron-induced signals in the coaxial cables.¹¹ The study of neutron-induced signals in the coaxial cables will continue on OMEGA. With an optimal cable, the upper-yield range of the NIF NBT is expected to be about 10^{17} .

Summary

A simple, low-cost, high-yield neutron bang time (HYNBT) detector has been developed and implemented on OMEGA. The HYNBT consists of three chemical-vapor-deposition (CVD) diamond detectors of different sizes and sensitivities placed in a lead-shielded housing. The HYNBT is located in a re-entrant tube 50 cm from the center of the target chamber. The HYNBT has been temporally cross-calibrated against the streak-camera-based neutron temporal diagnostic (NTD) for both D_2 and DT implosions. The HYNBT has an internal time resolution better than 20 ps. The three HYNBT channels can measure the neutron bang time in DT implosions over a yield range of 1×10^{10} to 1×10^{15} and above 5×10^{10} for D_2 implosions. The HYNBT can be implemented on the National Ignition Facility.

ACKNOWLEDGMENT

This work was supported by the U.S. Department of Energy Office of Inertial Confinement Fusion under Cooperative Agreement No. DE-FC52-92SF19460, the University of Rochester, and the New York State Energy Research and Development Authority. The support of DOE does not constitute an endorsement by DOE of the views expressed in this article.

REFERENCES

1. J. D. Lindl, *Inertial Confinement Fusion: The Quest for Ignition and Energy Gain Using Indirect Drive* (Springer-Verlag, New York, 1998).
2. R. A. Lerche *et al.*, *Rev. Sci. Instrum.* **59**, 1697 (1988).
3. N. Miyanaga *et al.*, *Rev. Sci. Instrum.* **61**, 3592 (1990).
4. C. Stoeckl, V. Yu. Glebov, J. D. Zuegel, D. D. Meyerhofer, and R. A. Lerche, *Rev. Sci. Instrum.* **73**, 3796 (2002).
5. R. A. Lerche, D. W. Phillion, and G. L. Tietbohl, *Rev. Sci. Instrum.* **66**, 933 (1995).
6. T. R. Boehly, D. L. Brown, R. S. Craxton, R. L. Keck, J. P. Knauer, J. H. Kelly, T. J. Kessler, S. A. Kumpan, S. J. Loucks, S. A. Letzring, F. J. Marshall, R. L. McCrory, S. F. B. Morse, W. Seka, J. M. Soures, and C. P. Verdon, *Opt. Commun.* **133**, 495 (1997).
7. J. M. Soures, R. L. McCrory, C. P. Verdon, A. Babushkin, R. E. Bahr, T. R. Boehly, R. Boni, D. K. Bradley, D. L. Brown, R. S. Craxton, J. A. Delettrez, W. R. Donaldson, R. Epstein, P. A. Jaanimagi, S. D. Jacobs, K. Kearney, R. L. Keck, J. H. Kelly, T. J. Kessler, R. L. Kremens, J. P. Knauer, S. A. Kumpan, S. A. Letzring, D. J. Lonobile, S. J. Loucks, L. D. Lund, F. J. Marshall, P. W. McKenty, D. D. Meyerhofer, S. F. B. Morse, A. Okishev, S. Papernov, G. Pien, W. Seka, R. Short, M. J. Shoup III, M. Skeldon, S. Skupsky, A. W. Schmid, D. J. Smith, S. Swales, M. Wittman, and B. Yaakobi, *Phys. Plasmas* **3**, 2108 (1996).
8. C. Stoeckl, J. A. Delettrez, J. H. Kelly, T. J. Kessler, B. E. Kruschwitz, S. J. Loucks, R. L. McCrory, D. D. Meyerhofer, D. N. Maywar, S. F. B. Morse, J. Myatt, A. L. Rigatti, L. J. Waxer, J. D. Zuegel, and R. B. Stephens, *Fusion Sci. Technol.* **49**, 367 (2006).
9. V. Yu. Glebov, C. Stoeckl, T. C. Sangster, S. Roberts, R. A. Lerche, and G. J. Schmid, *IEEE Trans. Plasma Sci.* **33**, 70 (2005).
10. Harris International, New York, NY 10036.
11. V. Yu. Glebov, R. A. Lerche, C. Stoeckl, G. J. Schmid, T. C. Sangster, J. A. Koch, T. W. Phillips, C. Mileham, and S. Roberts, presented at ICOPS 2005, International Conference on Plasma Sciences, Monterey, CA, 20–23 June 2005 (Paper 10281).
12. M. Moran, G. Mant, V. Glebov, C. Sangster, and J. Mack, presented at the 16th Annual Conference on High-Temperature Plasma Diagnostics, Williamsburg, VA, 7–11 May 2006 (Paper TP22).

Operation of Target Diagnostics in a Petawatt Environment

Introduction

Sensitive electronic detectors are difficult to operate in petawatt laser–target interaction experiments. The laser–plasma interaction at relativistic intensities ($>10^{18}$ W/cm²) in the focus of a high-energy, short-pulse laser system creates copious amounts of relativistic electrons ($E > 1$ MeV), hard x rays, and charged particles. Conversion efficiencies of up to 50% into MeV electrons¹ and 5% into MeV protons² have been reported. The energetic particles hit detectors inside the target chamber, creating a background signal and potentially damaging sensitive electronic structures. The MeV x rays easily escape the target chamber and impact diagnostic instrumentation inside the target area. Since the Compton-scattering cross section is significant at these energies, sidescattered and backscattered photons contribute to the background signal. X-ray fluorescence from high- Z material in the target area adds to this background. An electromagnetic pulse (EMP) is created when charged particles and x rays interact with structures inside the target chamber. This pulse will strongly affect and potentially damage any electronic device in or near the target chamber. EMP can also add background to electrical signals from detectors close to the target. It is conducted outside the target chamber through any cable or nonconducting window.³ Due to those problems, many diagnostics used in petawatt laser experiments rely on passive detectors such as x-ray film, nuclear activation,⁴ imaging plate,⁵ radio-chromic film,⁶ and CR39 track detectors.⁷ In many cases, electronic detectors provide higher sensitivity, higher dynamic range, better temporal resolution, and faster feedback after each laser shot. Strategies are being developed to mitigate the impact of EMP on electronic detectors inside and outside the target chamber and to shield them against background radiation. In this article, detector-development efforts for experimental campaigns at the petawatt facility^{8,9} of the Rutherford Appleton Laboratory (RAL) are presented showing successful approaches to improve the signal-to-background ratio on electronic detectors and to harden them against EMP. A variety of detectors, such as single-photon-counting, x-ray, charge-coupled-device (CCD) cameras, diamond x-ray detectors, and scintillator–photomultiplier neutron detectors, will be discussed. A new high-energy (1 kJ at 1 ps, 2.6 kJ at

10 ps) petawatt laser (OMEGA EP)^{10,11} is currently under construction at the Laboratory for Laser Energetics. Strategies to minimize the impact of EMP on diagnostics inside the target chamber of OMEGA EP will be presented.

Experimental Setup

The Rutherford Appleton Laboratory’s Vulcan petawatt laser delivers a 0.5-ps pulse of up to ~500 J in a 60-cm-diam beam, which is focused by an $f/3$ off-axis parabola into a <10 - μ m-diam focal spot. Due to losses in the compressor and wavefront aberrations, less than 50% of the laser energy is contained within the central portion of the focal spot, leading to an estimated maximum intensity on target of about 4×10^{20} W/cm². As seen in Fig. 107.31, the petawatt target chamber is well shielded by 10 cm of lead on top and on three sides. The access corridor to the target chamber entry doors, which are unshielded, is backed by a 10-cm lead, 60-cm-concrete curtain shield. The diagnostics under discussion were set up at different locations in the target area, on the target chamber, and in the target chamber (see Fig. 107.31). The single-photon-counting, x-ray, CCD camera was mounted 3.8 m from target chamber center (TCC) on a 1-m-long vacuum tube outside the target chamber wall. A chemical-vapor-deposition (CVD) diamond hard-x-ray (>50 -keV) detector was mounted either inside or outside the target chamber at ~1 m from the TCC. Diamond photoconductive devices (PCD’s) for soft x rays (<2 keV) were used either inside the target chamber at ~50 cm from TCC or at the target chamber wall at 2.8 m. A scintillator–photomultiplier neutron detector was placed at 6.5 m from TCC behind a second 20-cm-lead curtain shield. This curtain shield is set up to protect a large-area neutron scintillator array.¹²

Single-Photon-Counting CCD

In a single-photon-counting x-ray CCD spectrometer, the photon flux is attenuated so that every CCD pixel is hit by, at most, one photon. At moderate x-ray energies (<50 keV) a significant fraction of photons deposit all of their energy in one pixel; therefore, the histogram of the pixel values is proportional to the incident photon spectrum. This type of spectrometer has the benefit of requiring no alignment but can be affected by a

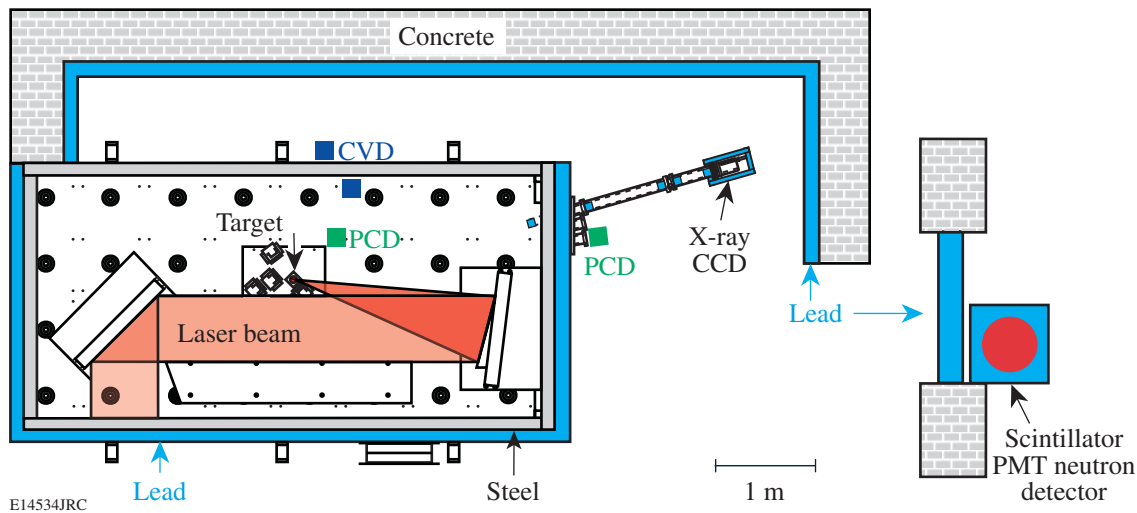


Figure 107.31

Overview of the target area at the RAL petawatt facility showing the shielding setup and layout of the x-ray CCD, CVD diamond, diamond PCD, and scintillator-photomultiplier detectors.

poor signal-to-background ratio. Detailed shielding strategies for single-photon-counting x-ray CCD spectrometers can be found in the literature.¹³ The most important finding reported was the importance of shielding not only the direct line of sight, but against Compton-scattered and fluorescence x rays from the side and back of the camera (see Fig. 107.31).

Diamond Hard-X-Ray Detector

CVD diamond detectors¹⁴ are an attractive choice as hard-x-ray or neutron detectors in high-energy, ultrafast laser-plasma experiments. CVD diamonds are radiation hard, thus able to cope with the large fluxes of x rays and particles. They are fast and have a large dynamic range, which makes them able to discriminate fast particles (x rays and electrons) from slower particles, such as protons and neutrons. The detector used in these experiments was made by DeBeer's Industrial Diamond Division by microwave-assisted plasma deposition as described in Ref. 11. The diamond wafer was cylindrical, 10 mm in diameter, and 1 mm thick, with 8-mm-diam Cr-Au (10/500 nm, respectively) contacts on both sides. The CVD detector was run at a 1000-V bias through a high-voltage, high-speed bias-tee,¹⁵ and the signals were recorded on a 1-GHz digital sampling scope.¹⁶ Figure 107.32 shows signals recorded from a CVD detector placed either inside the target chamber or outside the target chamber. The distance to TCC was ~ 1 m in both cases (see Fig. 107.31). To bring the signal to the outside of the chamber, an extra ~ 1 -m RG58 cable was connected to a BNC vacuum feedthrough. The cable run outside the target chamber into the oscilloscope was identical. The laser was set

to ~ 1 -ps pulse length at best focus. For the experiment with the detector inside the target chamber, a $360\text{-}\mu\text{m}$ CH/CD/CH foil was irradiated using 390 J of laser energy and a $140\text{-}\mu\text{m}$ CD foil was irradiated with 330 J laser energy with the detector outside the target chamber. The signal inside the target chamber is severely compromised by EMP noise pickup almost as high as the x-ray peak. The only noise seen in the signal outside the target chamber is the digitizing noise of the scope. Because of a lower scope sensitivity setting, the digitizing noise is higher

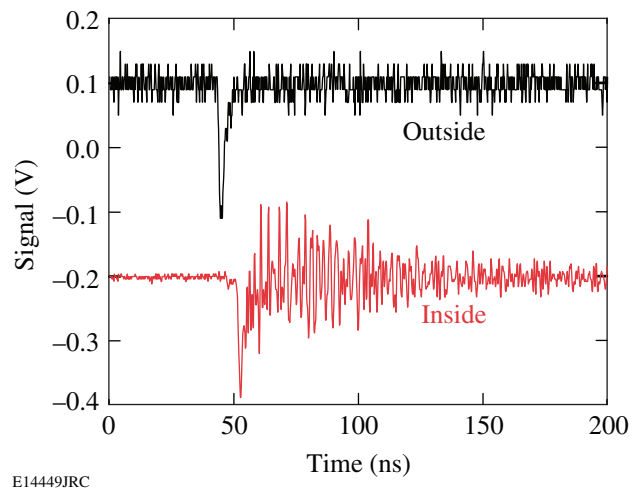


Figure 107.32

Signals from the CVD diamond hard-x-ray detector recorded at 1 m from the target inside and outside the target chamber.

on the outside. The timing difference in the x-ray peak is due to the different cable lengths to the oscilloscope. The fact that the x-ray signal experiences little change by moving the detector outside the target chamber, where the x rays are attenuated by an additional 1 cm of steel, shows that the x rays recorded by the CVD detectors are significantly above 100 keV.

Diamond Soft-X-Ray Detector

Diamond photoconductive devices (PCD's)¹⁷ are frequently used as soft-x-ray detectors (<2 keV) because they are sensitive ($\sim 6 \times 10^{-4}$ A/W) and very fast (<200 ps) and have a flat x-ray response and a high dynamic range. Because of the high band gap of 5.5 eV, they are not sensitive to laser light. A six-channel PCD array was used in these experiments, each detector consisting of a 0.5-mm- or 1-mm-thick, 1×3 -mm-area diamond mounted in a modified SMA connector¹⁸ [see Figs. 107.33(a) and 107.33(b)]. The detectors were biased through a custom-made six-channel bias-tee to 1000 V. Different-thickness CH and Al filters were used to modify the spectral response of the individual detectors. The detectors were fitted with a lead shield that limited the solid angle to an area close to the target [see Fig. 107.33(c)]. The PCD array was used either inside the target chamber at ~ 50 cm from TCC or on the target chamber wall at ~ 2.8 m (see Fig. 107.31). Figure 107.34 shows data from one channel on two shots recorded with the PCD array inside the target chamber, illustrating the benefit of the high dynamic

range of the diamond PCD. Both targets were CH/CD/CH foils of 360- μ m thickness irradiated with a 1-ps pulse at nominally best focus. The only apparent difference was the laser energy of 340 J in Fig. 107.34(a) and 500 J in Fig. 107.34(b). The first signal at 65 ns can be attributed to x rays from the target and changes by only a factor of 6 between the two shots. A second signal is seen around 100 ns attributed to protons coming from the target. This proton signal is not visible at all in Fig. 107.34(a) but completely saturated the detector in Fig. 107.34(b). The number of shots in this experimental campaign was very limited; therefore it was not possible to reproduce the second shot in Fig. 107.34(b) and use additional attenuation to prevent clipping on both signals. These large variations in the signals pose a significant danger to the recording system as shown in Fig. 107.35. In this case, the PCD array was mounted on the target chamber wall, which limited the x-ray signal to ~ 2 V in this shot, but the influx of protons was so intense that the PCD shorted completely and dumped all the charge present in the cable through the bias-tee into the input amplifier of the scope. In this case, the cable between the bias-tee and the detector was very short; consequently the energy flowing into the amplifier was limited so the scope recovered from this event. A longer cable or a less-resilient amplifier would have caused permanent damage to the oscilloscope. Because of the lower signal amplitudes, the PCD array is more susceptible to EMP pickup at the target chamber wall. Figure 107.36 shows signals from

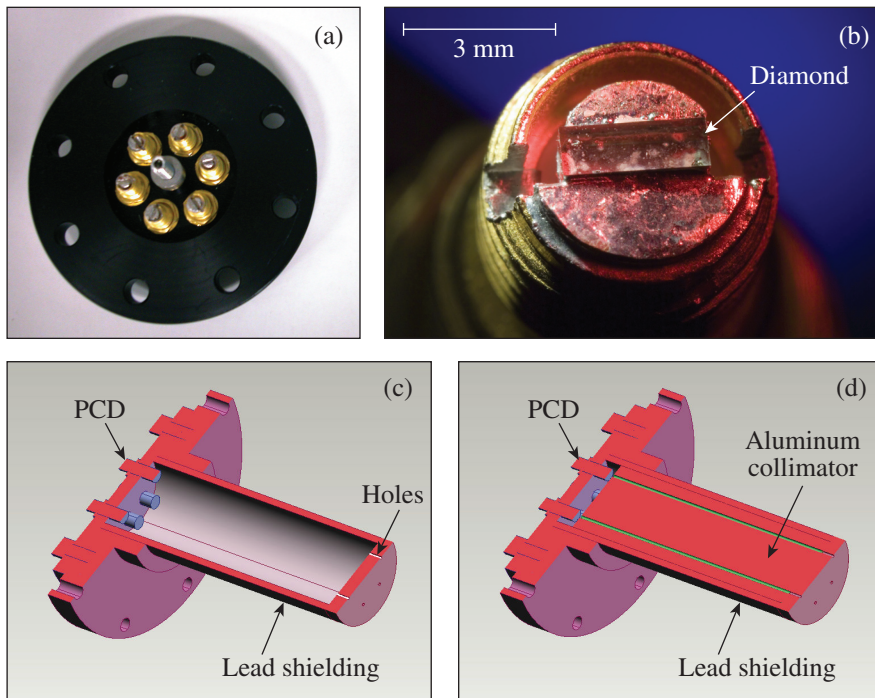
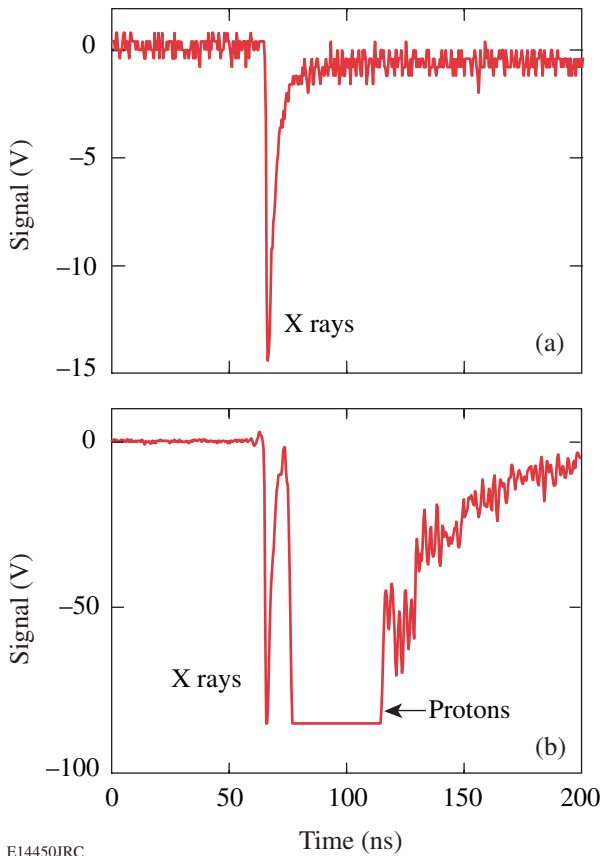


Figure 107.33

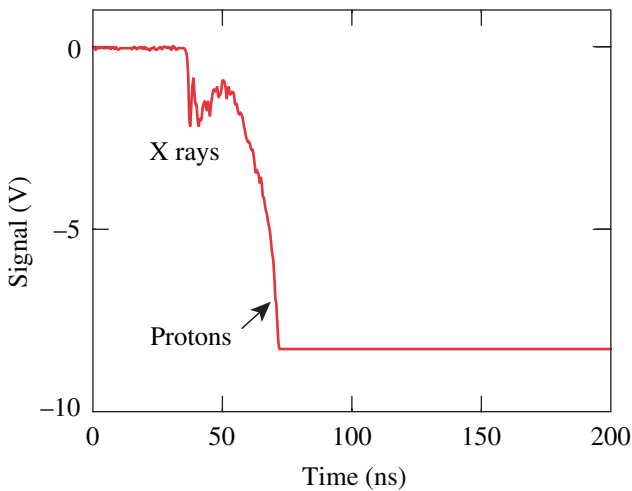
(a) Setup of the six-channel diamond PCD detector. (b) A $1 \times 1 \times 3$ -mm³ diamond is mounted in a modified SMA connector. (c) A lead collimator limits the solid angle to an area close to the target. (d) An additional aluminum collimator is inserted into the lead collimator for EMP shielding.

E14460JRC



E14450JRC

Figure 107.34 Data from one channel of the diamond PCD array mounted inside the target chamber from two shots on 360- μm -thick CH/CD/CH targets irradiated with a 1-ps pulse at best focus with (a) 340 J and (b) 500 J of laser energy.



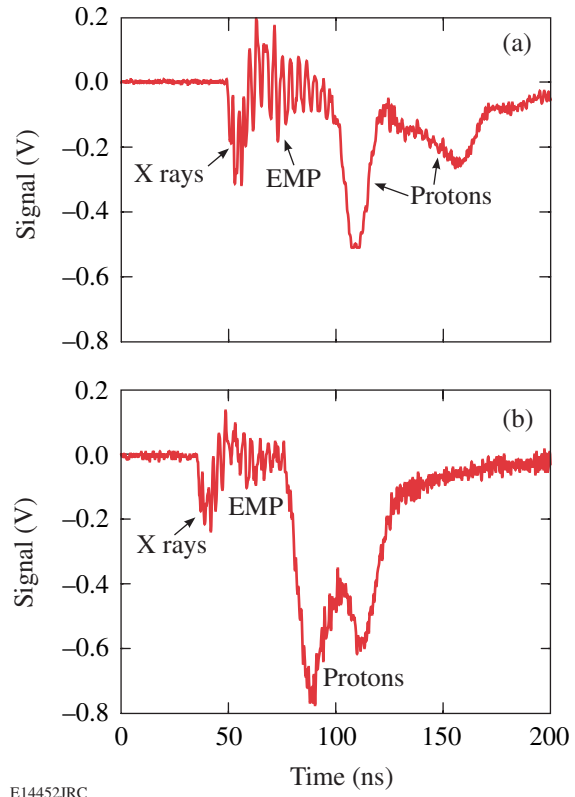
E14451JRC

Figure 107.35 Trace from one channel of the PCD array mounted on the target chamber wall, showing that the device shorts out at high proton fluxes.

one channel of the PCD array where the noise from the EMP is significant, (a) without and (b) with additional EMP shielding. The additional EMP shielding consisted of an Al cylinder with six holes for the x rays to reach the PCD array that fits inside the lead collimator [see Fig. 107.33(d)]. This shielding reduced the EMP signals, as seen in the traces between 50 to 100 ns, by roughly a factor of 2 from ~ 200 to ~ 100 mV. Since the primary x-ray peak at 50 ns is only ~ 200 mV, the shielding is not sufficient in this case, but this concept can be further optimized by lengthening the collimator and reducing the hole diameter, thus minimizing further the EMP energy that can couple into the detector.

Scintillator–Photomultiplier Detector

Scintillator–photomultiplier (PMT) detectors have been used extensively for neutron detection in inertial confinement fusion experiments.¹⁹ Since the cross section for a neutron interacting with matter is quite small and the number of neutrons produced in ultrafast laser–plasma interaction experiments is not very



E14452JRC

Figure 107.36 Signals from one PCD showing the EMP pickup of an (a) unshielded detector compared to (b) a detector with an additional Al collimator for EMP shielding.

large ($\sim 10^8$ neutrons have been reported²⁰), a large detector volume is required to obtain a measurable neutron signal. The detector used in these experiments has an 18-cm-diam, 10-cm-thick PILOT U²¹ scintillator coupled to an XP2020 PMT.²² A very thick, 5-cm lead shield placed around the scintillator and 25 cm toward the target is required to avoid saturation of the PMT from hard x rays because of its very high gain (of the order of 10^7), even though the interaction cross section of MeV x rays with the scintillator is quite low. Figure 107.37 shows a scintillator signal recorded from a neutron-producing 200- μm -thick CD target irradiated with 558 J of laser energy at 1 ps and best focus compared to a 25- μm Au foil irradiated by 500 J. Even with the very thick shielding, a significant signal from high-energy x rays is detected in both cases, whereas only the CD target data show a second structure ~ 100 ns later that can be attributed to neutrons of <20 -MeV energy. A peak from 2.45-MeV D₂ neutrons was not detected in these experiments; it would appear at ~ 340 ns in Fig. 107.37. Adding more lead does not significantly increase the signal-to-background ratio because the x-ray attenuation at the minimum of the lead x-ray attenuation cross section (2 to 5 MeV) is comparable to the neutron attenuation length at several-MeV neutron energy.

EMP Mitigation on OMEGA EP

OMEGA EP, a new high-energy petawatt laser system currently under construction at LLE,^{10,11} will provide two short-pulse (~ 1 - to 100-ps), 1053-nm beams with a maximum energy

of 2.6 kJ at 10 ps, limited only by the current damage threshold of the compression gratings. These short-pulse beams can be combined collinearly and coaxially for fast-ignitor channeling experiments in the OMEGA target chamber or sent to a new OMEGA EP target chamber. Both target chambers are 1.6-m-radius Al spheres of ~ 7.5 -cm thickness. Two additional long-pulse beams can provide up to ~ 6.5 kJ of 351-nm UV light with up to a 10-ns pulse length into the OMEGA EP target chamber. The two short-pulse beams can also be used as long-pulse UV beams in the OMEGA EP target chamber. The short-pulse beams are focused with an $f/2$ parabola to a <10 - μm -radius spot containing 80% of the energy. The intensity in the focal spot is predicted to be in excess of 3×10^{20} W/cm². A single OMEGA EP beam will have up to $5\times$ higher energy available compared to the Vulcan petawatt laser. Since both target chambers are of comparable volume, extensive efforts will be required to minimize background and mitigate EMP effects. EMP effects will be most severe for diagnostics, which are inserted into the target chamber using the OMEGA 10-in. manipulators (TIM's). For prompt electronic detectors inside the target chamber (e.g., the diamond PCD's discussed earlier), a grounding scheme is proposed that minimizes the potential for EMP pickup²³ (see Fig. 107.38). The sensor is housed inside a Faraday enclosure, which will be inserted through the TIM into the target chamber. The Faraday enclosure is grounded to the target chamber. The sensor package is electrically isolated inside the Faraday enclosure, and the coaxial signal cable is routed through an electrically conducting conduit into the recording device sitting inside a shielded and grounded diagnostic rack. Special care will be taken to minimize any apertures where electromagnetic energy could couple into the Faraday enclosure and the sensor package. Any currents induced by EMP inside the target chamber will flow through the Faraday enclosure into the target chamber and back to the target. Currents outside the target chamber will flow through the conduit, so the influence on the measurement through the coaxial cable will be minimized. Sensors that do not produce a prompt electrical signal at shot time (like CCD's or streak cameras) will use a different EMP shielding approach. The Faraday enclosure in these detectors will also serve as a pressure vessel to maintain atmospheric pressure around the readout and control electronics. Fiber optics will be used to transmit command information and data. A single dc voltage fed into the enclosure and converted into the required voltages inside the pressure vessels using shielded and filtered dc-dc converters will power these systems. Using a relatively high voltage of 28 V will limit any effects of EMP noise pickup on the feed lines even if it exceeds several volts for many milliseconds.

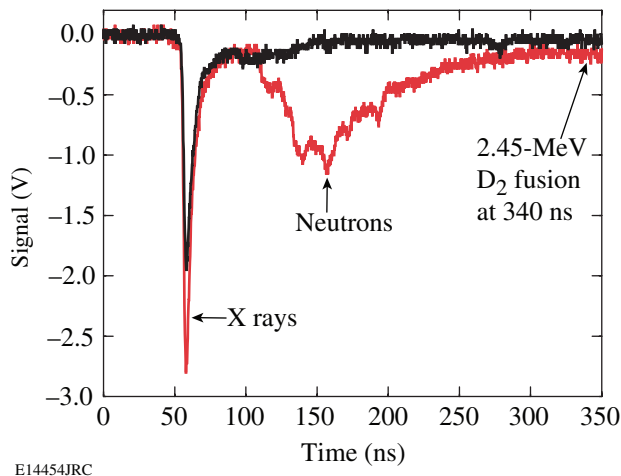


Figure 107.37
Neutrons were seen from CD targets using the scintillator-photomultiplier detector. Results from a non-neutron-producing Au target are shown for comparison.

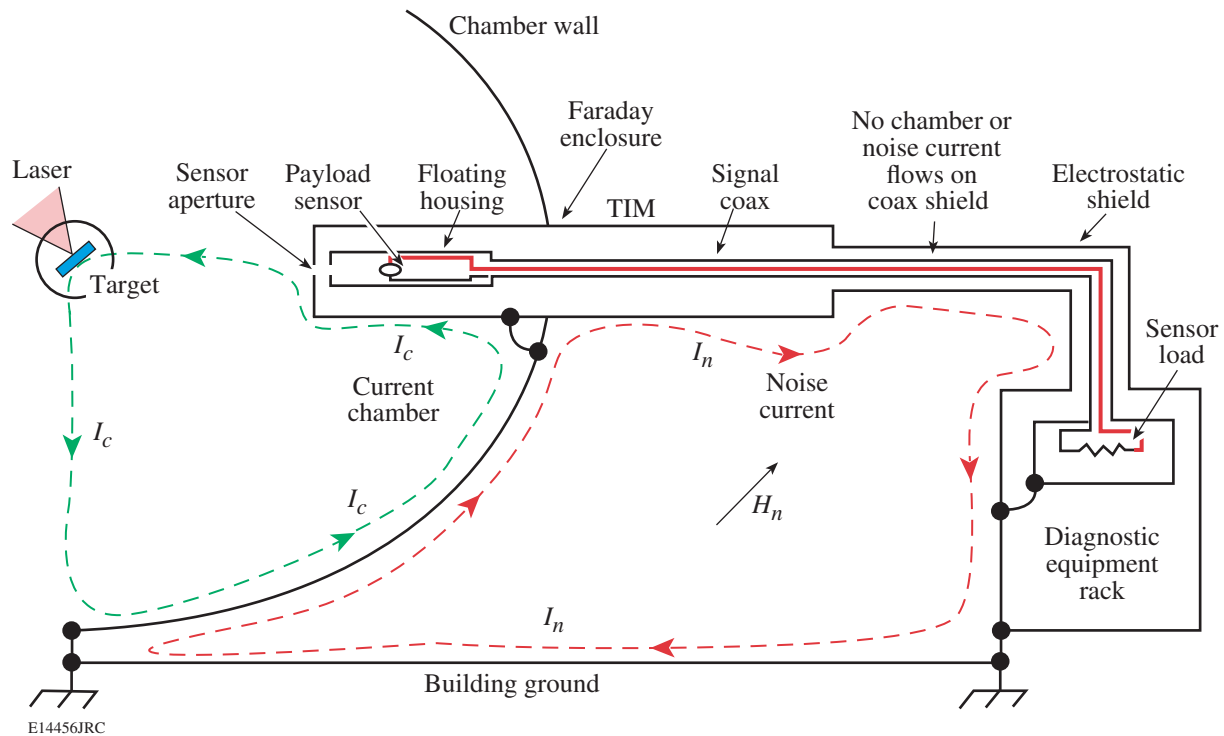


Figure 107.38
Proposed grounding and shielding for the TIM diagnostic-insertion setup on OMEGA EP.

Discussion

To minimize x-ray background in high-energy petawatt laser-interaction experiments, it is necessary to shield not only the direct line of sight, but also the full solid angle around the detector, because Compton-scattered and fluorescence photons can enter the detector from all sides. The high variability of the x rays or particles emitted from the target poses a significant risk to sensitive recording equipment, especially if a detector is run with a high bias voltage, like diamond PCD's, CVD diamond detectors, and certain photodiodes. EMP pickup is of special concern inside the target chamber, where EMP can easily overwhelm weak signals from detectors as seen with the PCD detectors on Vulcan. If possible it is much better to mount the detector outside the target chamber in a much lower EMP environment. These lessons learned from the RAL petawatt experiments will be applied in the experiments on the upcoming OMEGA EP high-energy petawatt facility, where optimized grounding strategies and detector configurations are being implemented.

ACKNOWLEDGMENT

This work was supported by the U.S. Department of Energy Office of Inertial Confinement Fusion under Cooperative Agreement No. DE-FC52-92SF19460, the University of Rochester, and the New York State Energy Research and Development Authority. The support of DOE does not constitute an endorsement by DOE of the views expressed in this article.

REFERENCES

1. K. Yasuike *et al.*, *Rev. Sci. Instrum.* **72**, 1236 (2001).
2. S. P. Hatchett *et al.*, *Phys. Plasmas* **7**, 2076 (2000).
3. J. L. Bourgade, V. Allouche, J. Baggio, C. Bayer, F. Bonneau, C. Chollet, S. Darbon, L. Disdier, D. Gontier, M. Houry, H. P. Jacquet, J.-P. Jadaud, J. L. Leray, I. Masclat-Gobin, J. P. Negre, J. Raimbourg, B. Villette, I. Bertron, J. M. Chevalier, J. M. Favier, J. Gazave, J. C. Gomme, F. Malaise, J. P. Seaux, V. Yu. Glebov, P. Jaanimagi, C. Stoeckl, T. C. Sangster, G. Pien, R. A. Lerche, and E. Hodgson, *Rev. Sci. Instrum.* **75**, 4204 (2004).
4. M. A. Stoyer, T. C. Sangster, E. A. Henry, M. D. Cable, T. E. Cowan, S. P. Hatchett, M. H. Key, M. J. Moran, D. M. Pennington, M. D. Perry, T. W. Phillips, M. S. Singh, R. A. Snavely, M. Tabak, and S. C. Wilks, *Rev. Sci. Instrum.* **72**, 767 (2001).

5. Y. Okano *et al.*, *J. Appl. Phys.* **95**, 2278 (2004).
6. R. A. Snavely, M. H. Key, S. P. Hatchett, T. E. Cowan, M. Roth, T. W. Phillips, M. A. Stoyer, E. A. Henry, T. C. Sangster, M. S. Singh, S. C. Wilks, A. MacKinnon, A. Offenberger, D. M. Pennington, K. Yasuike, A. B. Langdon, B. F. Lasinski, J. Johnson, M. D. Perry, and E. M. Campbell, *Phys. Rev. Lett.* **85**, 2945 (2000).
7. K. L. Lancaster, S. Karsch, H. Habara, F. N. Beg, E. L. Clark, R. Freeman, M. H. Key, J. A. King, R. Kodama, K. Krushelnick, K. W. D. Ledingham, P. McKenna, C. D. Murphy, P. A. Norreys, R. Stephens, C. Stoeckl, Y. Toyama, M. S. Wei, and M. Zepf, *Phys. Plasmas* **11**, 3404 (2004).
8. C. B. Edwards *et al.*, in *25th International Congress on High-Speed Photography and Photonics*, edited by C. Cavailler, G. P. Haddleton, and M. Hugenschmidt (SPIE, Bellingham, WA, 2003), Vol. 4948, pp. 444–451.
9. C. N. Danson *et al.*, in *Inertial Fusion Sciences and Applications 2001*, edited by K. A. Tanaka, D. D. Meyerhofer, and J. Meyer-ter-Vehn (Elsevier, Paris, 2002), pp. 479–483.
10. L. J. Waxer, D. N. Maywar, J. H. Kelly, T. J. Kessler, B. E. Kruschwitz, S. J. Loucks, R. L. McCrory, D. D. Meyerhofer, S. F. B. Morse, C. Stoeckl, and J. D. Zuegel, *Opt. Photonics News* **16**, 30 (2005).
11. C. Stoeckl, J. A. Delettrez, J. H. Kelly, T. J. Kessler, B. E. Kruschwitz, S. J. Loucks, R. L. McCrory, D. D. Meyerhofer, D. N. Maywar, S. F. B. Morse, J. Myatt, A. L. Rigatti, L. J. Waxer, J. D. Zuegel, and R. B. Stephens, *Fusion Sci. Technol.* **49**, 367 (2006).
12. J. L. Collier *et al.*, *Central Laser Facility Annual Report 2002/2003*, 168, Rutherford Appleton Laboratory, Chilton, Didcot, Oxon, England, RAL Report No. RAP-TR-2003-018 (2003).
13. C. Stoeckl, W. Theobald, T. C. Sangster, M. H. Key, P. Patel, B. B. Zhang, R. Clarke, S. Karsch, and P. Norreys, *Rev. Sci. Instrum.* **75**, 3705 (2004).
14. G. J. Schmid, R. L. Griffith, N. Izumi, J. A. Koch, R. A. Lerche, M. J. Moran, T. W. Phillips, R. E. Turner, V. Yu. Glebov, T. C. Sangster, and C. Stoeckl, *Rev. Sci. Instrum.* **74**, 1828 (2003).
15. Picosecond Pulse Labs, Boulder, CO 80301.
16. Oscilloscope Model No. TDS684, Tektronix, Inc., Beaverton, OR 97077.
17. D. R. Kania *et al.*, *Rev. Sci. Instrum.* **61**, 2765 (1990).
18. Alameda Applied Sciences Corporation, San Leandro, CA 94577.
19. M. D. Cable and M. B. Nelson, *Rev. Sci. Instrum.* **59**, 1738 (1988).
20. P. A. Norreys *et al.*, *Plasma Phys. Control. Fusion* **40**, 175 (1998).
21. Nuclear Enterprises Ltd., United Kingdom.
22. Koninklijke Philips Electronics N.V., The Netherlands.
23. M. E. Morris *et al.*, Lawrence Livermore National Laboratory, Livermore, CA, UCRL-TM-212140, NIF-0111782 (April 2005).

Gain Apodization in Highly Doped, Distributed-Feedback (DFB) Fiber Lasers

Introduction

Fiber lasers have been the subject of much research over the past ten years. They can provide high reliability, fiber compatibility, high output power, good beam quality, narrow bandwidth, low phase noise, and low relative intensity noise (RIN).^{1–4} These characteristics make them promising alternatives to solid-state and semiconductor lasers. Distributed-feedback (DFB) fiber lasers can be designed with a grating structure to provide high output power (up to 60 mW), single frequency,⁵ single polarization,⁶ and high optical signal-to-noise ratio (OSNR).⁶ DFB fiber lasers have been widely used in sensing,⁷ communication systems,^{8–11} and high-precision spectroscopy,¹² all of which require single-mode, single-frequency lasers.

To obtain higher-power DFB fiber lasers, doping levels have been increased to allow more pump light to be absorbed with the doping densities of commercial Yb-doped fibers approaching $1 \times 10^{25}/\text{cm}^3$ (e.g., INO, Nufern). With the commercial availability of 500-mW pump lasers, the absorption transition easily becomes saturated. As the majority of the pump light is absorbed or converted into lasing photons, however, the remainder of the fiber is essentially unpumped. The transition length between the pumped and unpumped regions is given by the small-signal absorption, which is of the order of a millimeter or less. This gain apodization effect with pumped and unpumped sections of the DFB laser has so far been neglected.

In this article, the effects of gain apodization in DFB fiber lasers are investigated. In particular, the impact on threshold behavior is explored along with its effect on output power and mode discrimination. In the following sections (1) the conventional model based on coupled-wave equations is reviewed and applied to our case of fiber lasers; (2) the physics of gain apodization in DFB lasers is explored and compared to conventional configurations; (3) the impact of gain apodization on phase-shifted DFB fiber lasers is investigated; (4) lasing thresholds and the output power ratio from both ends of the fiber lasers are analyzed; and, finally, (5) techniques for using gain apodization as an optimization tool are discussed.

Coupled-Wave Matrix Model

Although DFB lasers are widely used for single-mode operation, in general their mode spectrum is more complicated. In a uniform index-coupled DFB fiber laser without phase shift or end mirrors, DFB lasers can operate in one of two degenerate longitudinal modes symmetrically located along the Bragg frequency of the grating. Nominally, only a single mode runs because of fabrication imperfections that cause slight asymmetry.

Coupled-mode theory^{13,14} can be used to analyze the threshold behavior in simple DFB lasers. Figure 107.39 is a schematic of the coupling between forward and backward waves in waveguides induced by periodic modulation of the refractive index n . For a uniform fiber grating with uniform gain, the coupled-wave equations can be written as¹⁵

$$\begin{aligned} dE_A/dz &= \kappa \exp[i(2\Delta\beta z - \phi)]E_B + gE_A, \\ dE_B/dz &= \kappa \exp[-i(2\Delta\beta z - \phi)]E_A - gE_B, \end{aligned} \quad (1)$$

where E_A and E_B are the complex amplitudes of the forward and backward propagating waves, $\Delta\beta = \beta - m\pi/\Lambda$ is the propagation constant difference between the wave in the z direction and the m^{th} Bragg frequency of the grating ($m = 1$ for first-order gratings), ϕ is the wave phase at the position $z = 0$, κ is the coupling coefficient between the forward and

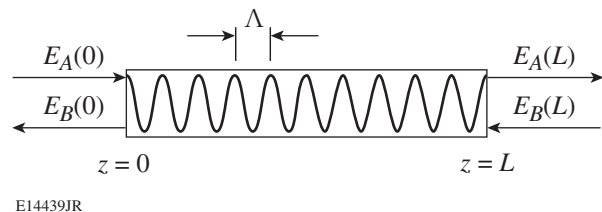


Figure 107.39
Schematic of coupled waves in periodic active waveguides.

backward waves in the grating, and g is the gain coefficient of the active medium collocated with the grating. In the absence of reflections from either side of the structures, Eq. (1) can be solved analytically.

To model a more complicated structure, e.g., where the gain is not constant along z , a matrix method^{15,16} can be used to concatenate the solutions to Eq. (1). In this formalism, a non-uniform periodic structure is broken into segments of uniform period structures each with the solution

$$\begin{bmatrix} E_A(z_{j+1}) \\ E_B(z_{j+1}) \end{bmatrix} = \begin{pmatrix} F_{11}^j & F_{12}^j \\ F_{21}^j & F_{22}^j \end{pmatrix} \begin{bmatrix} E_A(z_j) \\ E_B(z_j) \end{bmatrix}, \quad (2)$$

where the matrix elements are the solutions to Eq. (1) given by

$$\begin{aligned} F_{11}^j &= \left[\cosh(\gamma_j L_j) + i \Delta \beta_j' L_j \sinh(\gamma_j L_j) / (\gamma_j L_j) \right] \\ &\quad \times \exp(i \beta_B^j L_j), \\ F_{12}^j &= -\kappa_j L_j \sinh(\gamma_j L_j) \exp[-i(\beta_B^j L_j + \phi_j)] / (\gamma_j L_j), \\ F_{21}^j &= -\kappa_j L_j \sinh(\gamma_j L_j) \exp[i(\beta_B^j L_j + \phi_j)] / (\gamma_j L_j), \\ F_{22}^j &= \left[\cosh(\gamma_j L_j) - i \Delta \beta_j' L_j \sinh(\gamma_j L_j) / (\gamma_j L_j) \right] \\ &\quad \times \exp[-i(\beta_B^j L_j)], \end{aligned} \quad (3)$$

and where $\Delta \beta_j' = \Delta \beta_j + i g_j$, $\gamma_j^2 = \kappa_j^2 - (\Delta \beta_j')^2$, and $\beta_B^j = \pi / \Lambda_j$. With this formalism the active gratings can be split into N sections where the total matrix will be $F_t = F_N F_{N-1} \dots F_2 F_1$. For a nonuniform DFB fiber laser, the coupling coefficient κ and gain coefficient g can change with the position z . For DFB fiber lasers without a phase shift, the phase terms in Eq. (3) can be written as $\phi^k = \phi^{k-1} + 2\beta_B^k L^{k-1}$, where $k = 1, 2, \dots, N$. For phase-shifted DFB fiber lasers, the phase terms in Eq. (3) can be written as $\phi^k = \phi^{k-1} + 2\beta_B^k L^{k-1} + \Delta \phi^k$, $k = 1, 2, \dots, N$. Adding the boundary conditions $E_A(0) = E_B(L) = 0$, the gain threshold condition can be obtained from the relation $F_{t11} = 0$ (Ref. 15). Nominally, this relation will produce a mode spectrum with different modes appearing at different frequencies $\Delta \beta$.

For high-power operation, it is desirable not only to have a low threshold but also to have most of the light coming out of

only one side of the cavity. By using the total matrix F_t , the output power ratio from both ends of the fiber can be written as

$$\frac{P_1}{P_2} = \left| \frac{E_B(0)}{E_A(L)} \right|^2 = |F_{21}^2|, \quad (4)$$

where P_1/P_2 presents the ratio of the power coupling out at $z = 0$, as compared to $z = L$.

Gain-Apodization Physics

To understand the physics introduced by gain apodization, the formalism in the previous section is applied to three cases. In all cases, the grating strength κ and period Λ are kept constant and no phase shift will be included. The peak reflectivity of the grating is determined by $R = \tanh^2(\kappa L)$, and, so that the desired generality is not lost, typical values for κ and L are chosen. In the following sections, the coupling coefficient of the fiber grating is $\kappa = 1 \text{ cm}^{-1}$ and the grating lengths are 3 cm in most cases. Since the length under which the gain will drop from its maximum value to zero is less than 1 mm, the gain apodization along the z axis will be approximated by a step function. The gain-apodized DFB fiber laser is schematically shown in Fig. 107.40(a), where the L_1 section is highly doped with the uniform gain coefficient g and L_2 has no gain. This case will be compared to two other cases: The first, a DFB fiber laser of length L_1 and uniform gain but no unpumped section, is shown in Fig. 107.40(b). The second case, shown in

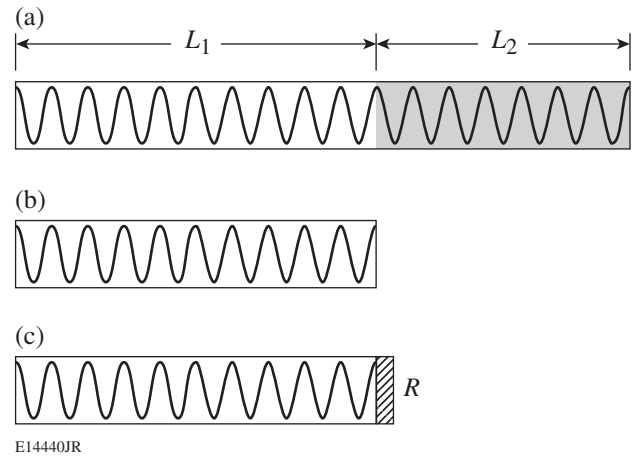


Figure 107.40

Schematic of the (a) gain-apodized DFB fiber laser, (b) uniform DFB fiber laser, and (c) uniform DFB fiber laser with end reflector $R_2 = \tanh^2(\kappa L_2)$. The shaded regions indicate sections with no gain.

Fig. 107.40(c), is the same laser as shown in Fig. 107.40(b) but with a reflector at the end of the cavity where the grating would be in the apodized case. The reflectivity value is chosen to be the peak reflectivity of the unpumped fiber grating of the case shown in Fig. 107.40(a), namely, $R_2 = \tanh^2(\kappa L_2)$. This value was chosen to directly compare to the apodized case shown in Fig. 107.40(a).

The gain thresholds for these cases where $L_1 = 2.5$ cm and $L_2 = 0.5$ cm are shown in Fig. 107.41. The horizontal axis is the normalized frequency $\Delta\beta L$ (where $L = L_1 + L_2$), while the vertical axis is the normalized gain threshold $g_{th}L_1$. The gain is normalized with L_1 since the value of gL_1 relates to the pump power. The mode spectra of the three different lasers are nearly identical since the lasing cavities are of nearly equal length. When compared to the short DFB laser, the gain-apodized DFB lasers show a nearly 30% reduction in lasing threshold due to its passive grating section. The DFB with the reflector similarly shows a reduction in the lasing threshold for its first-order mode. However, the threshold reduction applies significantly to all modes since the reflector is spectrally uniform. For the gain-apodized DFB laser, whose passive section has spectral dependence, the additional reflector also aids in modal discrimination with higher-order modes.

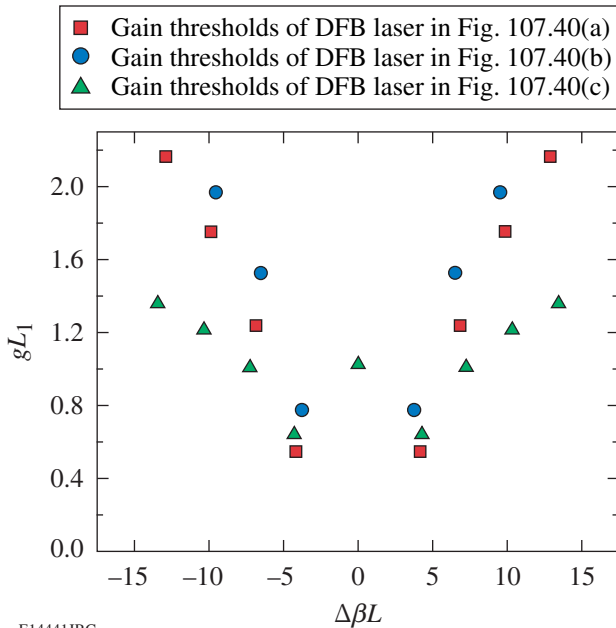


Figure 107.41
Gain thresholds of the DFB fiber laser configurations shown in Fig. 107.40.

It is also important to note that although the passive grating system introduces system asymmetry, the zeroth-order mode cannot reach the lasing threshold since the phase of the transition between the two sections is maintained. Nevertheless, Fig. 107.41 demonstrates the advantage of using gain apodization for reduced lasing threshold without the penalty of decreased spectral purity.

Figure 107.42 shows the gain threshold for DFB lasers plotted with the Bragg grating reflection spectrum to understand the interplay of active versus grating length. The grating reflection spectrum can be formulated as¹⁷

$$R_g(\delta) = |r_g(\delta)|^2 = \left| \frac{i\kappa \sin(qL)}{q \cos(qL) - i\delta \sin(qL)} \right|^2, \quad (5)$$

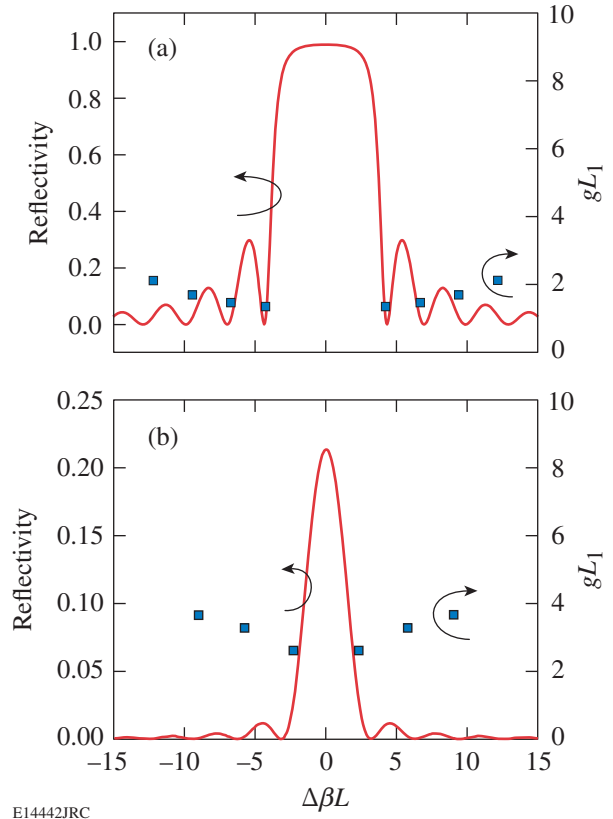


Figure 107.42
(a) The modal frequencies of a gain-apodized DFB fiber laser with $L_1 = 0.5$ cm, $L_2 = 2.5$ cm, and a reflection spectrum of a 3-cm fiber Bragg grating. (b) The modal frequencies of a 0.5-cm uniform-gain DFB fiber laser and a reflection spectrum of a 0.5-cm fiber Bragg grating.

where $\delta(\omega) = (\bar{n}/c)(\omega - \omega_B) \equiv \beta(\omega) - \beta_B$, κ is the coupling coefficient of the grating, L is the grating length, and $q = \pm \sqrt{\delta^2 - \kappa^2}$.

To exaggerate the physics, the active portion of the gain-apodized DFB fiber laser is chosen to be $L_1 = 0.5$ cm with the passive portion longer, $L_2 = 2.5$ cm. The mode spectrum of this laser and the corresponding reflectivity of a 3-cm fiber Bragg grating (FBG) are shown in Fig. 107.42(a). For comparison, Fig. 107.42(b) shows the mode spectrum of a conventional 0.5-cm-long DFB laser with the reflectivity spectrum of a 0.5-cm FBG. It is clear from these figures that the mode spectrum of the gain-apodized laser is determined by the entire grating rather than only by the active portion.

Figure 107.43 shows the lowest modal gain threshold versus gain length L_1 for the gain-apodized DFB laser. From this figure, it is clear that the minimum threshold for L_1/L is close to 0.7; the gain threshold is 17.9% less compared to the uniform DFB fiber laser ($L_1/L = 1$). For gain lengths L_1/L less than unity, the longitudinal distribution of light extends into the unpumped region, creating an effectively higher reflectivity. Since no gain is extracted from this region, the effective grating strength is increased, thus creating a lower gain threshold. For values of L_1/L that are too small (less than 0.7 in this case), the grating-length product becomes too small to produce sufficient reflection, effectively increasing the laser threshold via reduced feedback. Figure 107.43 demonstrates that gain apodization can decrease the laser threshold if properly tailored.

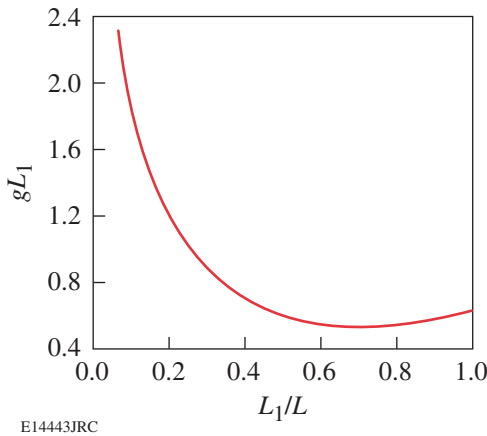


Figure 107.43
The gain thresholds of the lowest-order mode as a function of gain-apodization profile.

Impact on Phase-Shifted DFB Lasers

It is convenient to avoid mode degeneracy by introducing a phase shift in the middle of the grating. As is well known, the π -phase shift will enable a narrowband filter in the grating-forbidden band, thereby allowing the zeroth-order mode to have a low lasing threshold.¹⁸ Considering the influence of this geometry, it is instructive to understand the role of gain apodization on phase-shifted DFB fiber lasers.

Figures 107.44(a) and 107.44(b) show the lowest-mode gain threshold and the mode discrimination of the uniform-gain, phase-shifted DFB fiber lasers. As before, the total cavity length L is 3 cm and the coupling coefficient is 1 cm^{-1} . The results show that the apodization with the lowest gain threshold also has nearly the largest mode discrimination. Slightly different to the optimum L_1/L of 0.7 for a normal DFB laser in Fig. 107.43, the optimum gain-apodization profile will be where

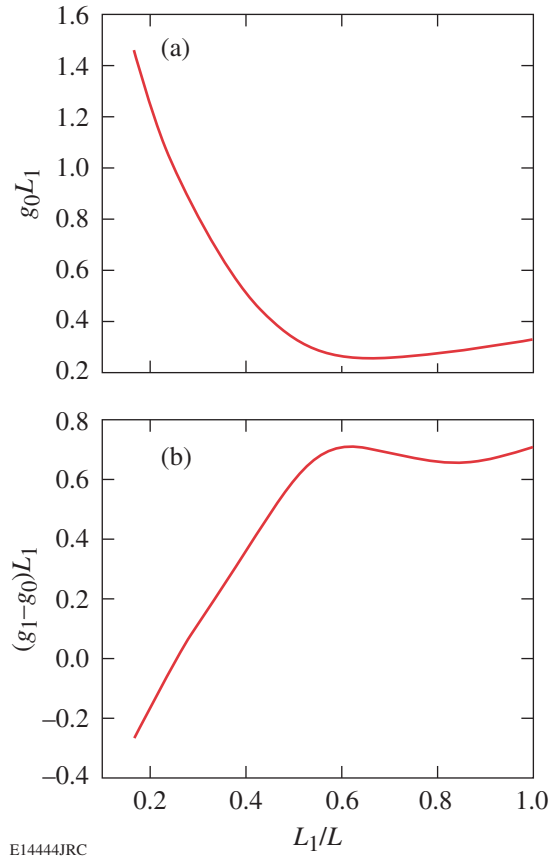


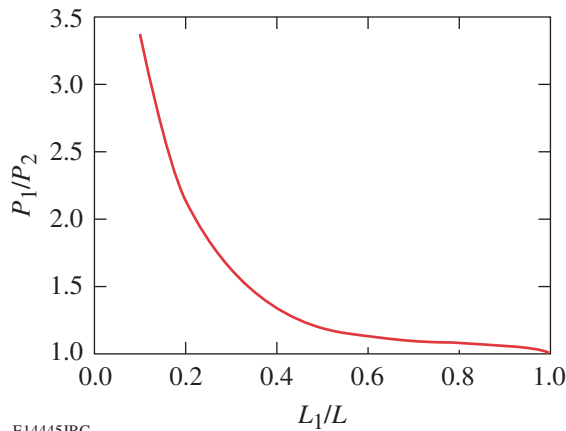
Figure 107.44
(a) The lowest-mode gain threshold versus L_1/L . (b) The mode-1 and mode-0 gain threshold difference versus L_1/L .

L_1/L is close to 0.6. From Fig. 107.44(a), the gain threshold can be reduced 21.2%, compared to the normal phase-shifted DFB fiber laser with nearly the same modal discrimination, as shown in Fig. 107.44(b).

Since the gain apodization has introduced system asymmetry, the output power ratio from both ends of the laser will also be modified. To investigate these characteristics, the output power ratio of Eq. (4) is plotted against the apodized gain length L_1/L in Fig. 107.45. The power ratio from both ends of the fiber changes monotonically with the apodization gain length L_1/L . Higher output power from the pumped end of the cavity can be obtained at the optimum pumped length L_1/L for the minimum threshold shown in Fig. 107.44(a); the power ratio can be increased by 12.4%. This asymmetry, combined with the 21.2% threshold reduction, can lead to a substantial increase in output power solely because of gain apodization.

Discussion and Conclusions

It was shown in the previous section that gain apodization can have a beneficial impact on phase-shifted DFB lasers. It has been previously shown that DFB laser performance can be improved by changing the location of the phase shift and varying κ along the laser axis.^{19,20} To obtain the highest single-frequency output from DFB fiber lasers, the gain-apodization length, phase-shift location, and coupling coefficient profile must all be optimized. While this presents a challenging numerical problem, genetic algorithms have proven useful in optimizing laser and amplifier designs.^{21–23}



E14445JRC

Figure 107.45

The output power ratio from the fiber ends versus L_1/L .

While the lasing threshold itself will determine the gain-apodization profile for a given DFB laser, this effect can be intentionally introduced. Two separate sections of photosensitive fiber, only one of which is doped with active ions to provide gain, can be spliced together before a grating is written into the fiber. In this way, the independent control of the gain profile, grating strength, and phase-shift location can be used to optimize of DFB laser performance.

In conclusion, the effects of gain apodization in highly doped DFB fiber lasers were investigated. In particular, apodization of the longitudinal gain profile resulted in a lower lasing threshold than a laser with uniform gain without the penalty of modal discrimination. For the case studied, the lasing threshold was reduced by almost 18% for a conventional DFB laser and over 21% for a DFB laser with a π -phase shift. Furthermore, the longitudinal asymmetry introduced by gain apodization yielded a significantly higher ratio of output power from opposite ends of the laser. Methods of engineering and optimizing such a gain-apodized DFB fiber laser were also discussed.

ACKNOWLEDGMENT

This work was supported by the U.S. Department of Energy Office of Inertial Confinement Fusion under Cooperative Agreement No. DE-FC52-92SF19460, the University of Rochester, and the New York State Energy Research and Development Authority. The support of DOE does not constitute an endorsement by DOE of the views expressed in this article.

REFERENCES

1. G. A. Cranch, M. A. Englund, and C. K. Kirkendall, *IEEE J. Quantum Electron.* **39**, 1579 (2003).
2. K. H. Ylä-Jarkko, *IEEE Photonics Technol. Lett.* **15**, 191 (2003).
3. L. Qiu *et al.*, *IEEE Photonics Technol. Lett.* **16**, 2592 (2004).
4. S. Foster, *IEEE J. Quantum Electron.* **40**, 1283 (2004).
5. Ch. Spiegelberg *et al.*, in *Optical Fiber Communications Conference, 2003*, OSA Trends in Optics and Photonics (TOPS), Vol. 86 (Optical Society of America, Washington, DC, 2003).
6. M. Ibsen *et al.*, in *Lasers and Electro-Optics, 1999 (CLEO '99)* (Optical Society of America, Washington, DC, 1999), Paper CWE4, pp. 245–246.
7. J. T. Kringlebotn, W. H. Loh, and R. I. Laming, *Opt. Lett.* **21**, 1869 (1996).
8. R. Gross, R. Olshansky, and M. Schmidt, *IEEE Photonics Technol. Lett.* **2**, 66 (1990).
9. U. Gliese, E. L. Christensen, and K. E. Stubkjaer, *J. Lightwave Technol.* **9**, 779 (1991).

10. J. Hübner, P. Varming, and M. Kristensen, *Electron. Lett.* **33**, 139 (1997).
11. F. Liu *et al.*, *Electron. Lett.* **36**, 620 (2000).
12. R. Böhm *et al.*, *Opt. Lett.* **18**, 1955 (1993).
13. H. Kogelnik and C. V. Shank, *J. Appl. Phys.* **43**, 2327 (1972).
14. W. Streifer, D. R. Scifres, and R. D. Burnham, *IEEE J. Quantum Electron.* **QE-13**, 134 (1977).
15. M. Yamada and K. Sakuda, *Appl. Opt.* **26**, 3474 (1987).
16. S. Radic, N. George, and G. P. Agrawal, *IEEE J. Quantum Electron.* **31**, 1326 (1995).
17. G. P. Agrawal, *Lightwave Technology: Components and Devices* (Wiley, Hoboken, NJ, 2004).
18. G. P. Agrawal, J. E. Geusic, and P. J. Anthony, *Appl. Phys. Lett.* **53**, 178 (1988).
19. K. Yelen, L. M. B. Hickey, and M. N. Zervas, *IEEE J. Quantum Electron.* **40**, 711 (2004).
20. K. Yelen, M. N. Zervas, and L. M. B. Hickey, *J. Lightwave Technol.* **23**, 32 (2005).
21. C. Cheng, Z. Xu, and C. Sui, *Opt. Commun.* **227**, 371 (2003).
22. M. Gao *et al.*, *Opt. Express* **12**, 5603 (2004).
23. C. Cheng and S. He, *Microw. Opt. Technol. Lett.* **22**, 343 (1999).

Publications and Conference Presentations

Publications

- R. Betti and C. Zhou, "Low-Adiabatic Implosions for Fast-Ignition Inertial Confinement Fusion," *J. Phys. IV France* **133**, 379 (2006).
- T. R. Boehly, E. Vianello, J. E. Miller, R. S. Craxton, T. J. B. Collins, V. N. Goncharov, I. V. Igumenshchev, D. D. Meyerhofer, D. G. Hicks, P. M. Celliers, and G. W. Collins, "Shock-Timing Experiments Using Double-Pulse Laser Irradiation," *Phys. Plasmas* **13**, 056303 (2006) (invited).
- J. Bromage, J. D. Zuegel, S.-W. Bahk, D. S. Vickery, L. J. Waxer, D. Irwin, V. Bagnoud, R. Boni, M. D. Moore, R. Jungquist, and C. Stoeckl, "High-Intensity Laser Diagnostics for OMEGA EP," *J. Phys. IV France* **133**, 705 (2006).
- J. Bunkenburg, T. J. Kessler, W. Skulski, and H. Huang, "Phase-Locked Control of Tiled-Grating Assemblies for Chirped-Pulse-Amplified Lasers Using a Mach-Zehnder Interferometer," *Opt. Lett.* **31**, 1561 (2006).
- S. W. Culligan, A. C.-A. Chen, J. U. Wallace, K. P. Klubek, C. W. Tang, and S. H. Chen, "Effect of Hole Mobility Through Emissive Layer on Temporal Stability of Blue Organic Light-Emitting Diodes," *Adv. Funct. Mater.* **16**, 1481 (2006).
- J. L. DeCiantis, F. H. Séguin, J. A. Frenje, V. Berube, M. J. Canavan, C. D. Chen, S. Kurebayashi, C. K. Li, J. R. Rygg, B. E. Schwartz, R. D. Petrasso, J. A. Delettrez, S. P. Regan, V. A. Smalyuk, J. P. Knauer, F. J. Marshall, D. D. Meyerhofer, S. Roberts, T. C. Sangster, C. Stoeckl, K. Mikaelian, H. S. Park, and H. F. Robey, "Proton Core Imaging of the Nuclear Burn in Inertial Confinement Fusion Implosions," *Rev. Sci. Instrum.* **77**, 043503 (2006).
- D. H. Edgell, R. S. Craxton, L. M. Elasky, D. R. Harding, L. S. Iwan, R. L. Keck, L. D. Lund, S. J. Verbridge, M. D. Wittman, A. Warrick, T. Brown, and W. Seka, "Three-Dimensional Characterization of Cryogenic Target Ice Layers Using Shadowgraph Views," *Fusion Sci. Technol.* **49**, 616 (2006).
- D. H. Edgell, W. Seka, R. S. Craxton, L. M. Elasky, D. R. Harding, R. L. Keck, L. D. Lund, and M. D. Wittman, "Characterization of Cryogenic Direct-Drive ICF Targets During Layering Studies and Just Prior to Shot Time," *J. Phys. IV France* **133**, 903 (2006).
- V. N. Goncharov, O. V. Gotchev, R. L. McCrory, P. W. McKenty, D. D. Meyerhofer, T. C. Sangster, S. Skupsky, and C. Cherfils-Clerouin, "Ablative Richtmyer-Meshkov Instability: Theory and Experimental Results," *J. Phys. IV France* **133**, 123 (2006).
- D. R. Harding, D. D. Meyerhofer, S. J. Loucks, L. D. Lund, R. Janezic, L. M. Elasky, T. H. Hinterman, D. H. Edgell, W. Seka, M. D. Wittman, R. Q. Gram, D. Jacobs-Perkins, R. Early, T. Duffy, and M. J. Bonino, "Forming Cryogenic Targets for Direct-Drive Experiments," *Phys. Plasmas* **13**, 056316 (2006) (invited).
- M. Haurylau, S. P. Anderson, K. L. Marshall, and P. M. Fauchet, "Electrical Tuning of Photonic-Bandgap Structures in Silicon," *SPIE Newsroom, Nanotechnology*, April 2006, <http://newsroom.spie.org>.
- A. Jukna, I. Barboy, G. Jung, A. Abrutis, X. Li, D. Wang, and R. Sobolewski, "Electric Transport Properties of $\text{YBa}_2\text{Cu}_3\text{O}_{7-\delta}$ Thin-Film Bridges with Laser-Written Channels of Easy Vortex Motion," *J. Appl. Phys.* **99**, 113902 (2006).
- J. H. Kelly, L. J. Waxer, V. Bagnoud, I. A. Begishev, J. Bromage, B. E. Kruschwitz, T. J. Kessler, S. J. Loucks, D. N. Maywar, R. L. McCrory, D. D. Meyerhofer, S. F. B. Morse, J. B. Oliver, A. L. Rigatti, A. W. Schmid, C. Stoeckl, S. Dalton, L. Folsbee, M. J. Guardalben, R. Jungquist, J. Puth, M. J. Shoup III, D. Weiner, and J. D. Zuegel, "OMEGA EP: High-Energy Petawatt Capability for the OMEGA Laser Facility," *J. Phys. IV France* **133**, 75 (2006).

- C. Kim, A. Trajkovska, J. U. Wallace, and S. H. Chen, "New Insight into Photoalignment of Liquid Crystals on Coumarin-Containing Polymer Films," *Macromolecules* **39**, 3817 (2006).
- A. K. Knight and D. R. Harding, "Modeling Polymer Vapor Deposition: PMDA-ODA Poly(amic Acid)," *Fusion Sci. Technol.* **49**, 728 (2006).
- A. Korneev, O. Minaeva, I. Rubtsova, I. Milostnaya, G. Chulkova, B. Voronov, K. Smirnov, V. Seleznev, G. Gol'tsman, A. Pearlman, W. Słysz, A. Cross, P. Alvarez, A. Verevkin, R. Sobolewski, "Superconducting Single-Photon Ultrathin NbN Film Detector," *Quantum Electron.* **35**, 698 (2005).
- B. E. Kruschwitz, R. Jungquist, J. Qiao, S. Abbey, S. E. Dean, D. N. Maywar, M. D. Moore, L. J. Waxer, and M. E. Wilson, "Large-Aperture Deformable Mirror Correction of Tiled-Grating Wavefront Error," *J. Phys. IV France* **133**, 645 (2006).
- C. K. Li and R. D. Petrasso, "Energy Deposition of MeV Electrons in Compressed Target of Fast-Ignition Inertial Confinement Fusion," *Phys. Plasmas* **13**, 056314 (2006).
- S. G. Lukishova, N. Lepeshkin, R. W. Boyd, and K. L. Marshall, "Far-Field Patterns from Dye-Doped Planar-Aligned Nematic Liquid Crystals Under Nanosecond Laser Irradiation," *Mol. Cryst. Liq. Cryst.* **453**, 393 (2006).
- S. G. Lukishova and A. W. Schmid, "Near-Field Optical Microscopy of Defects in Cholesteric Oligomeric Liquid Crystal Films," *Mol. Cryst. Liq. Cryst.* **454**, 417 (2006).
- S. G. Lukishova, R. P. Knox, P. Freivald, A. McNamara, R. W. Boyd, C. R. Stroud, Jr., A. W. Schmid, and K. L. Marshall, "Single-Photon Source for Quantum Information Based on Single Dye Molecule Fluorescence in Liquid Crystal Host," *Mol. Cryst. Liq. Cryst.* **454**, 403 (2006).
- J. A. Marozas, F. J. Marshall, R. S. Craxton, I. V. Igumenshchev, S. Skupsky, M. J. Bonino, T. J. B. Collins, R. Epstein, V. Yu. Glebov, D. Jacobs-Perkins, J. P. Knauer, R. L. McCrory, P. W. McKenty, D. D. Meyerhofer, S. G. Noyes, P. B. Radha, T. C. Sangster, W. Seka, and V. A. Smalyuk, "Polar-Direct-Drive Simulations and Experiments," *Phys. Plasmas* **13**, 056311 (2006) (invited).
- F. J. Marshall, R. S. Craxton, M. J. Bonino, R. Epstein, V. Yu. Glebov, D. Jacobs-Perkins, J. P. Knauer, J. A. Marozas, P. W. McKenty, S. G. Noyes, P. B. Radha, W. Seka, S. Skupsky, and V. A. Smalyuk, "Polar-Direct-Drive Experiments on OMEGA," *J. Phys. IV France* **133**, 153 (2006).
- K. L. Marshall, K. Adelsberger, G. Myhre, and D. W. Griffin, "The LCPDI: A Compact and Robust Phase-Shifting, Point-Diffraction Interferometer Based on Dye-Doped LC Technology," *Mol. Cryst. Liq. Cryst.* **454**, 23 (2006).
- K. L. Marshall, G. Painter, K. Lotito, A. G. Noto, and P. Chang, "Transition Metal Dithiolene Near-IR Dyes and Their Applications in Liquid Crystal Devices," *Mol. Cryst. Liq. Cryst.* **454**, 47 (2006) (invited).
- R. L. McCrory, D. D. Meyerhofer, S. J. Loucks, S. Skupsky, R. Betti, T. R. Boehly, T. J. B. Collins, R. S. Craxton, J. A. Delettrez, D. H. Edgell, R. Epstein, K. A. Fletcher, C. Freeman, J. A. Frenje, V. Yu. Glebov, V. N. Goncharov, D. R. Harding, I. V. Igumenshchev, R. L. Keck, J. D. Kilkenny, J. P. Knauer, C. K. Li, J. Marciante, J. A. Marozas, F. J. Marshall, A. V. Maximov, P. W. McKenty, S. F. B. Morse, J. Myatt, S. Padalino, R. D. Petrasso, P. B. Radha, S. P. Regan, T. C. Sangster, F. H. Séguin, W. Seka, V. A. Smalyuk, J. M. Soures, C. Stoeckl, B. Yaakobi, and J. D. Zuegel, "Progress in Direct-Drive Inertial Confinement Fusion Research at the Laboratory for Laser Energetics," *J. Phys. IV France* **133**, 59 (2006).
- J. B. Oliver and D. Talbot, "Optimization of Deposition Uniformity for Large-Aperture National Ignition Facility Substrates in a Planetary Rotation System," *Appl. Opt.* **45**, 3097 (2006).
- W. T. Shmayda, S. J. Loucks, R. Janezic, T. W. Duffy, D. R. Harding, and L. D. Lund, "Tritium Operations at the Laboratory for Laser Energetics," *Fusion Sci. Technol.* **49**, 851 (2006).
- S. Skupsky, R. S. Craxton, F. J. Marshall, R. Betti, T. J. B. Collins, R. Epstein, V. N. Goncharov, I. V. Igumenshchev, J. A. Marozas, P. W. McKenty, P. B. Radha, J. D. Kilkenny, D. D. Meyerhofer, T. C. Sangster, and R. L. McCrory, "Polar Direct Drive—Ignition at 1 MJ," *J. Phys. IV France* **133**, 233 (2006).
- W. Słysz, M. Węgrzecki, J. Bar, P. Grabiec, M. Górská, V. Zwiller, C. Latta, P. Bohi, I. Milostnaya, O. Minaeva, A. Antipov, O. Okunev, A. Korneev, K. Smirnov, B. Voronov,

N. Kaurova, G. Gol'tsman, A. Pearlman, A. Cross, I. Komissarov, A. Verevkin, and R. Sobolewski, "Fiber-Coupled Single-Photon Detectors Based on NbN Superconducting Nanostructures for Practical Quantum Cryptography and Photon-Correlation Studies," *Appl. Phys. Lett.* **88**, 261113 (2006).

V. A. Smalyuk, O. Sadot, R. Betti, V. N. Goncharov, J. A. Delettrez, D. D. Meyerhofer, S. P. Regan, T. C. Sangster, and D. Shvarts, "Rayleigh–Taylor Growth Measurements of Three Dimensional Modulations in a Nonlinear Regime," *Phys. Plasmas* **13**, 056312 (2006) (invited).

C. Stoeckl, J. A. Delettrez, J. H. Kelly, T. J. Kessler, B. E. Kruschwitz, S. J. Loucks, R. L. McCrory, D. D. Meyerhofer, D. N. Maywar, S. F. B. Morse, J. Myatt, A. L. Rigatti, L. J. Waxer, J. D. Zuegel, and R. B. Stephens, "High-Energy Petawatt Project at the University of Rochester's Laboratory for Laser Energetics," *Fusion Sci. Technol.* **49**, 367 (2006).

W. Theobald, K. Akli, R. Clarke, J. A. Delettrez, R. R. Freeman, S. Glenzer, J. Green, G. Gregori, R. Heathcote, N. Izumi, J. A. King, J. A. Koch, J. Kuba, K. Lancaster, A. J. MacKinnon,

M. Key, C. Mileham, J. Myatt, D. Neely, P. A. Norreys, H.-S. Park, J. Pasley, P. Patel, S. P. Regan, H. Sawada, R. Shepherd, R. Snavelly, R. B. Stephens, C. Stoeckl, M. Storm, B. Zhang, and T. C. Sangster, "Hot Surface Ionic Line Emission and Cold K-Inner Shell Emission from Petawatt-Laser-Irradiated Cu Foil Targets," *Phys. Plasmas* **13**, 043102 (2006).

J. U. Wallace and S. H. Chen, "Simplified Scheme for Deterministic Synthesis of Chiral-Nematic Glassy Liquid Crystals," *Ind. Eng. Chem. Res.* **45**, 4494 (2006).

J. D. Zuegel, V. Bagnoud, J. Bromage, I. A. Begishev, and J. Puth, "High-Performance OPCPA Laser System," *J. Phys. IV France* **133**, 701 (2006).

J. D. Zuegel, S. Borneis, C. Barty, B. LeGarrec, C. Danson, N. Miyanaga, P. K. Rambo, C. LeBlanc, T. J. Kessler, A. W. Schmid, L. J. Waxer, J. H. Kelly, B. Kruschwitz, R. Jungquist, E. Moses, J. Britten, I. Jovanovic, J. Dawson, and N. Blanchot, "Laser Challenges for Fast Ignition," *Fusion Sci. Technol.* **49**, 453 (2006).

Forthcoming Publications

I. V. Igumenshchev, "Three-Dimensional Simulations of Spherical Accretion Flows with Small-Scale Magnetic Fields," to be published in the *Astrophysical Journal*.

Z. Jiang and J. R. Marciante, "Mode-Area-Scaling of Helical-Core, Dual-Clad Fiber Lasers and Amplifiers Using an Improved Bend Loss Model," to be published in the *Journal of the Optical Society of America B*.

J. R. Marciante and J. D. Zuegel, "High-Gain, Polarization-Preserving, Yb-Doped Fiber Amplifier for Low-Duty-Cycle Pulse Amplification," to be published in *Applied Optics*.

J. A. Marozas, "Fourier-Transform-Based Continuous Phase-Plate Design Technique: A High-Pass Phase-Plate Design as an Application for OMEGA and the NIF," to be published in the *Journal of the Optical Society of America A*.

S. N. Shafir, J. C. Lambropoulos, and S. D. Jacobs, "A Magnetorheological Polishing–Based Approach for Studying Precision Microground Surfaces of Tungsten Carbides," to be published in *Precision Engineering*.

W. Słysz, M. Węgrzecki, J. Bar, P. Grabiec, M. Górska, V. Zwiller, C. Latta, P. Bohi, A. J. Pearlman, A. S. Cross, D. Pan, J. Kitaygorsky, I. Komissarov, A. Verevkin, I. Milostnaya, A. Korneev, O. Minayeva, G. Chulkova, K. Smirnov, B. Voronov, G. N. Gol'tsman, and R. Sobolewski, "Fiber-Coupled, Single-Photon Detector Based on NbN Superconducting Nanostructures for Quantum Communications," to be published in the *Journal of Modern Optics*.

Conference Presentations

S. G. Lukishova, A. W. Schmid, R. S. Knox, P. Freivald, L. Bissell, R. W. Boyd, C. R. Stroud, Jr., and K. L. Marshall, "Deterministically Polarized, Room-Temperature Source of Single Photons," Workshop on Linear Optical Quantum Information Processing, Baton Rouge, LA, 10–12 April 2006.

C. Wu and D. R. Harding, "Chemical Vapor Deposition of Carbon Nanotube-Reinforced Polymer Composites," 2006 MRS Spring Meeting, San Francisco, CA, 17–21 April 2006.

A. K. Knight, F.-Y. Tsai, T. N. Blanton, D. R. Harding, and S. H. Chen, "Optimizing the Vapor Deposition Method of Making Polyimide," 12th Meeting of the Symposium on Polymers for Microelectronics, Wilmington, DE, 3–5 May 2006.

The following presentations were made at the 16th Topical Conference on High-Temperature Diagnostics, Williamsburg, VA, 7–11 May 2006:

V. Yu. Glebov, D. D. Meyerhofer, T. C. Sangster, C. Stoeckl, S. Roberts, C. A. Barrera, J. R. Celeste, C. J. Cerjan, L. S. Dauffy, D. C. Eder, R. L. Griffith, S. W. Haan, B. A. Hammel, S. P. Hatchett, N. Izumi, J. R. Kimbrough, J. A. Koch, O. L. Landen, R. A. Lerche, B. J. MacGowan, M. J. Moran, E. W. Ng, T. W. Phillips, P. M. Song, R. Tommassini, B. K. Young, S. E. Caldwell, G. P. Grim, S. C. Evans, J. M. Mack, T. J. Sedillo, M. D. Wilke, D. C. Wilson, C. S. Young, D. Casey, J. A. Frenje, C. K. Li, R. D. Petrasso, F. H. Séguin, J. L. Bourgade, L. Disdier, M. Houry, I. Lantejoulé, O. Landoas, G. A. Chandler, G. W. Cooper, R. J. Leeper, R. E. Olson, C. L. Ruiz, M. A. Sweeney, S. P. Padalino, C. Horsfield, and B. A. Davis, "Development of Nuclear Diagnostics for the National Ignition Facility" (invited).

V. Yu. Glebov, C. Stoeckl, T. C. Sangster, C. Mileham, and R. A. Lerche, "High-Yield Bang Time Detector for the OMEGA Laser."

J. P. Knauer, F. J. Marshall, B. Yaakobi, D. Anderson, B. A. Schmitt, K. M. Chandler, S. A. Pikuz, T. A. Shelkovenko, M. D. Mitchell, and D. A. Hammer, "Response Model for Kodak Biomax-MS Film to X Rays."

F. J. Marshall, J. P. Knauer, D. Anderson, and B. A. Schmitt, "Absolute Calibration of Kodak Biomax-MS Film to X Rays in the 1.5- to 8-keV Range."

C. Stoeckl, V. Yu. Glebov, P. A. Jaanimagi, D. D. Meyerhofer, T. C. Sangster, M. Storm, S. Sublett, W. Theobald, M. H. Key, A. J. MacKinnon, P. K. Patel, D. Neely, and P. A. Norreys, "Operation of Target Diagnostics in a Petawatt Environment" (invited).

The following presentations were made at the Glass and Optical Materials Division Spring 2006 Meeting, Greenville, SC, 16–19 May 2006:

J. E. DeGroot, A. E. Marino, J. P. Wilson, and S. D. Jacobs, "The Role of Nanodiamond Abrasives in Optical Glass Removal with Magnetorheological Finishing (MRF)."

J. E. DeGroot, J. P. Wilson, T. M. Pfuntner, and S. D. Jacobs, "Incorporating Optical Glass Chemical Durability into a Glass Removal Model for Magnetorheological Finishing (MRF)."

The following presentations were made at CLEO/QELS 2006, Long Beach, CA, 21–26 May 2006:

W. R. Donaldson, D. N. Maywar, R. G. Roides, J. R. Marcianti, J. H. Kelly, J. D. Zuegel, and R. L. Keck, "High-Bandwidth, Pulse-Shape Control on a Frequency-Tripled Multiterawatt Solid-State Laser."

C. Dorrer and J. D. Zuegel, "Design and Analysis of Beam Apodizers Using Error Diffusion."

S. G. Lukishova, A. W. Schmid, R. S. Knox, P. Freivald, L. Bissell, R. W. Boyd, C. R. Stroud, Jr., and K. L. Marshall, "Deterministically Polarized, Room-Temperature Source of Single Photons Based on a Single-Emitter Fluorescence in Aligned Liquid Crystal Hosts."

J. R. Marciante, W. A. Bittle, and J. D. Zuegel, "Subpicosecond Jitter from a Precision Optical Triggering and Timing System Without Active Stabilization."

A. K. Knight, F.-Y. Tsai, and D. R. Harding, "Using Experiments and Calculations to Analyze Gas Flow and Surface Reaction in the Vapor Deposition of a Copolymer," FLUENT 2006 CFD Summit, Monterey, CA, 22–24 May 2006.

The following presentations were made at the 36th Anomalous Absorption Conference, Jackson Hole, WY, 4–9 June 2006:

R. S. Craxton, F. J. Marshall, M. J. Bonino, R. Epstein, V. Yu. Glebov, J. A. Marozas, S. G. Noyes, and V. A. Smalyuk, "An Update on Polar-Direct-Drive Experiments on OMEGA."

A. V. Maximov, J. Myatt, and R. W. Short, "Transport Near Critical Density Surface in Direct-Drive ICF Plasmas."

J. Myatt, A. V. Maximov, and R. W. Short, "Laboratory Astrophysics of e^+e^- Pair-Plasma Production on OMEGA EP."

W. Seka, V. N. Goncharov, J. A. Delettrez, R. W. Short, and R. S. Craxton, "Laser Absorption in Spherical Target Experiments on OMEGA."

R. W. Short and J. Myatt, "Filamentation of Fast-Ignition Transport in Plasmas: Spatial Growth and Absolute Modes."

The following presentations were made at the 29th ECLIM, Madrid, Spain, 11–16 June 2006:

R. L. McCrory, "Highlights of the History of the University of Rochester's Laboratory for Laser Energetics."

R. L. McCrory, "Present and Future Research at the Laboratory for Laser Energetics."

R. Betti, K. Anderson, T. R. Boehly, T. J. B. Collins, R. S. Craxton, J. A. Delettrez, D. H. Edgell, R. Epstein, V. Yu. Glebov, V. N. Goncharov, D. R. Harding, R. L. Keck, J. H. Kelly, J. P. Knauer, S. J. Loucks, J. A. Marozas, F. J. Marshall, A. V. Maximov, D. N. Maywar, R. L. McCrory, P. W. McKenty, D. D. Meyerhofer, J. Myatt, P. B. Radha, S. P. Regan, C. Ren, T. C. Sangster, W. Seka, S. Skupsky, V. A. Smalyuk, J. M. Soures, C. Stoeckl, W. Theobald, B. Yaakobi, C. Zhou, J. D. Zuegel, C. K. Li, R. D. Petrasso, F. H. Séguin, and J. A. Frenje, "Progress in Hydrodynamic Theory and Experiments for Direct-Drive and Fast-Ignition Inertial Confinement Fusion," 33rd European Physical Society Conference on Plasma Physics, Rome, Italy, 19–23 June 2006 (invited).

A. Melchior, T. R. Boehly, and J. E. Miller, "High-Pressure and Temperature Equation-of-State Studies Using Laser-Driven Shocks," Gordon Research Conference on High Pressure, Biddleford, ME, 25–30 June 2006.

W. Seka, "Overview of the LLE Effort in Support of the U.S. National HED and ICF Programs," JOWOG 37, Aldermaston, UK, 26–30 June 2006.

UNIVERSITY OF
ROCHESTER